COMPARATIVE STUDY OF CURVATURE INDUCED IMPROVEMENT IN MASS TRANSFER AND FOULING

LAKSHMI BALASUBRAMANIAM

(B.Eng ., (Hons), NUS)

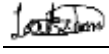## A THESIS SUBMITTED

FOR THE DEGREE OF MASTER OF ENGINEERING

DEPARTMENT OF MECHANICAL ENGINEERING

NATIONAL UNIVERSITY OF SINGAPORE

2016

DECLARATION

I hereby declare that the thesis is my original work and it has been written by me in its entirety. I have duly acknowledged all the sources of information which have been used in the thesis.

This thesis has also not been submitted for any degree in any university previously.

Lakshmi Balasubramaniam

28th September 2016

ACKNOWLEDGEMENTS

Contents

Summary

Mixing is a transport phenomenon which can lead to effects such as reaction and property changes of the reactants involved in this process. In a macroscale there are several ways to achieve this phenomenon through processes such as diffusion, advection, and Taylor dispersion. However, these macro scale micromixers can't be shrunk down to a microscale as surface effects are more dominant over volume effects at this level due to their dependency on length scale. Besides the dominance of surface effects, laminar flow regime poses as a challenge in designing micromixers since convective forces start to dominate diffusion effects beyond a certain Reynolds number thereby limiting the mixing performance of micromixers at higher Reynolds numbers. This is a major constraint for microreactor applications in the chemical engineering industry.

In this study the varying degree of mixing performance in different curvature profiles, such as a serpentine, saw tooth, U-shape, square curve and spiral channel have been studied by correlating mixing performance to the swirling strength of flow within these microchannels. Since swirling strength looks at the strength of vortex core within the microchannel it can act as an indicator of the strength of vortices formed within these microchannels. Having found that a spiral channel to be the best performing curvature variant the cross sectional geometry of the spiral channel was varied to study its impact on the strength of Dean vortices. From this it was understood that spiral channels with a semi-circular and trapezoidal cross-sectional profile have a higher swirling strength than traditional square shaped spiral channels which in turn improves the mixing performance to a value greater than 90% at Reynolds number >30 which can be assumed to be complete mixing according to previous studies.

Based on these results the different curvature designs were also compared for their varying degree of fouling resistance through microscopy experiments. As in the case of mixing performance, the spiral channel has a higher fouling resistance in comparison to the other designs such as saw tooth, serpentine, U shape and square curve design. This can be attributed back to the strength of Dean vortices which generate high shear stress along the channel walls preventing the dissolved particles from depositing along the channel.

Both mixing and fouling resistance studies show that a spiral channel can be effectively employed in microreactor applications with minimal damage through fouling and higher mixing performance rates in comparison to the other curvature designs. In addition a spiral channel occupies a smaller foot print area in comparison to their straight channel equivalents thereby minimizing the amount of material required for their fabrication. This strong understanding of mass transfer can also be applied in heat transfer applications while designing microscale heat sinks or heat exchangers which promotes modular design for higher efficiency.

LIST OF TABLES

LIST OF FIGURES

List of Symbols and Acronyms

a	Time differential of fouling resistance
A	Area of interest
A_{132}	Hamaker constant
c	Concentration of bulk fluid
C_b	Bulk concentration of fouling material
D	Diffusion coefficient
De	Dean number
D_h	Hydraulic diameter
d_p	Particle diameter
F_{EDL}	Electric double layer force
F_{vw}	Van der Waal's force
k	Mass transfer coefficient
L_m	Laminar mixing length
$\overline{m}$	Mass flux
MP	Mixing performance
P_e	Péclet number
$\dot{q}$	Heat flux at the wall
R	Radius of curvature
Re	Reynolds number of fluid
R_f	Fouling resistance
R_{ep}	Particle Reynolds number

Sh	Sherwood number
T	Bulk fluid temperature
T_w	Wall temperature
v	Fluid velocity
V_f	Fluid velocity
v_p	Particle velocity

Greek symbols

K	Debye Huckel parameter
κ^{-1}	Debye length
ρ_p	Density of particle
ρ_f	Density of fluid
N	Kinematic viscosity
λ_c	London characteristic wavelength
ϕ_D	Mass deposition rate per unit area
ϕ_R	Mass removal rate per unit area
ε_o	Permittivity of vacuum
ε	Relative permittivity of water
Ψ	Steam function
Ψ_s	Surface potential
k_f	Thermal conductivity of foulant
μ_f	Viscosity of bulk fluid
μ	Viscosity of particle
τ_w	Wall shear stress

Chapter 1

Introduction

1.1. Micromixers

Mixing in miniaturized scales is important in various analytical applications such as, biosensors[2], biological applications[3], chemical synthesis[4], polymerisation and extraction[5] within microreactors to name a few. The use of materials in smaller quantities would also play an important role in various thermal and chemical reactions which require fast results[6,7]. Flow introduced through such channels are briefly divided into two categories, laminar and turbulent flow based on their Reynolds number which represents the effect of viscous and inertial forces acting on the fluid. In general flow with a Re <2300 is considered to be laminar while flow with Re> 2300 is considered to be in the transitional followed by turbulent region of flow where Reynolds number (Re) is defined as below.

$$Re = \frac{Inertial\ forces}{Viscous\ forces} = \frac{\rho v D_h}{\mu} \tag{1}$$

where, D_h is the hydraulic diameter, ρ is the density of fluid being used, v the flow velocity and μ the dynamic viscosity of fluid being used. Hydraulic diameter of an irregular shape is obtained through the equation as below:

$$D_h = \frac{4A}{P}$$
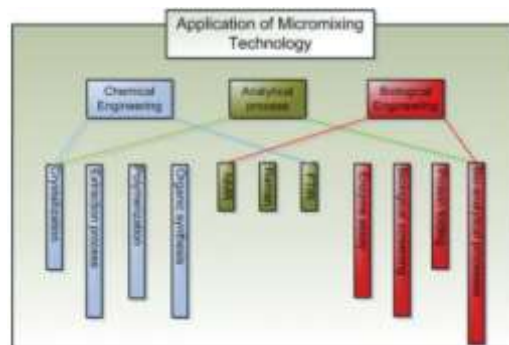
Figure 1: Classification of micromixing technologies[8]

At microscale, flow is basically laminar and mixing is governed by convection-diffusion equations, which causes the mixing between fluids to be dictated primarily by diffusion of molecules at lower Reynolds

number (Re < 100), while at higher Reynolds number, inertial forces dominate the flow leading to turbulent flow. However operating microchannels at such large Reynolds number with high velocities would require very large pumping power[9]. In microscales, large Péclet number indicates slow diffusion along the fluid layers as denoted below:

$$P_e = \frac{(advective\ transport)}{diffusive\ transport} = v * \frac{D_h}{D} \qquad (2)$$

where D_h could represent either the hydraulic diameter or the transverse diffusive length and D the molecular diffusivity. Diffusion being a nonlinear process the diffusion length is defined as:

$$x^2 = 2Dt \qquad (3)$$

Thus, for uniaxial flow the laminar mixing length is proportional to the Péclet number as:

$$L_m = P_e * D_h \qquad (4)$$

This shows that we need to employ longer channels to obtain desirable mixing performance as the timescale of diffusive terms are much lower than the convective terms. Operating the microchannels at a Re > 2300, leads to a larger pressure drop due to chaotic and unpredictable nature of the flow hence various geometrical modifications are employed as alternative ways to enhance rapid mixing, thereby reducing the mixing length and time required for complete mixing.

As a result micromixers are classified into two main categories based on the method employed to enhance mixing as active (activation through an external source of energy) and passive mixers (based on geometrical modifications).

1.2. Fouling in microchannels

Fouling is defined as the accumulation and deposition of particles in a fluid when it flows or when it is stagnant. Industrial water is known to carry trace amounts of particles along with it which results in the deposition of these particle along the flow path. Over time accumulation of these particles can result in

maldistribution of flow and flow disturbances which in turn affects performance of the device. This has typically been a problem in large scale heat exchangers which make use of metallic surfaces with sea water as their working fluid. Sea water carries numerous salts and algae with it resulting in particle deposition on these metallic surfaces or surface corrosion resulting in reduced surface area available for heat transfer thereby affecting heat transfer performance of the device. This is a well-studied problem among heat exchanger users and there are several ways to mitigate these problems such as:

1) Surface coating: Coating the surface with a hydrophobic polymeric layer prevents particle adhesion

2) Designing to improve flow profile: Using special design features in the heat exchanger can prevent fouling, for instance industries use spiral heat exchangers while operating highly viscous working fluids such as tar with very high particle content so as to minimize the effect of corrosion and facilitate easy flow path.

3) Material selection: Suitable materials with superior corrosion resistance and fouling resistance can be selected depending on the constituents of the working fluid.

On an average industrial countries loose about 0.25-0.3% of their GNP (gross national product)[10] due to fouling of these exchangers. Although they can be regularly cleaned the associated costs are very high along with downtime of the equipment and associated losses. Heat exchangers have also been oversized by about 30% with about 25% capital cost to compensate for the deleterious effects of fouling which results in extra material cost, transportation, delivery and miscellaneous cost[11] thereby driving research on how to reduce or mitigate fouling.

However when we move to microscale devices this becomes more critical due to the size and working range of these devices. With channel dimensions usually less than 1-2mm clogged particles would result in flow maldistribution, increased pressure drop, and leakage of the device due to this increased pressure drop. Miniaturization has several advantages as they occupy less foot print area, smaller volumes of fluid while providing faster reaction rates and quicker response owing to the miniaturization. This also increases the

3

surface area to volume ratio of the microchannel device due to miniaturization which increases the effective mass and heat transfer surface area resulting in superior or comparable performance to large scale devices. The miniaturization of devices has enabled us to perform multiple reactions simultaneously which is useful in those systems with fast reaction kinetics and high temperature dependence which requires the reaction to be completed in small time frames so as to avoid clogging or accumulation of the products. [12]

1.3.Problem statement and Thesis organization

In many heat exchanger or heat sink studies, we are often faced with the dilemma of capturing accurate and consistent temperature and pressure drop values which would be useful in developing new designs and configurations of heat sinks. The main aim of this work is to study the mixing between two fluids within different microchannel designs. While most studies observe mixing through top view imaging, in this study we have used a confocal microscope to visualize flow profile along the channel cross-section thereby giving an accurate prediction of mixing between two fluids. The flow field observed through imaging work was then correlated to a numerical model for validation. This method of studying mixing within microchannels would be useful in developing microchannel designs for lab on a chip devices and heat transfer studies. Experimentally evaluating different design profiles for heat transfer studies would be hard owing to the experimental errors and time taken for each study. This method of characterizing mixing can be used as a basis to develop heat sinks as mass transfer and heat transfer are linearly related to each other.

Another issue faced by most microscale heat exchanger devices during service is in the form of fouling where particles are trapped due to the development of dead zones and retarding velocity zones which act as an attractant for these water borne particles. Through this work we have identified that fouling in microchannels can be minimized through geometric modifications, which has not been explored before. Geometric modifications can help in controlling flow profile thereby minimizing the amount of dead zones while improving the mixing performance.

The remaining chapters in this thesis have been organized as follows:

Chapter 2 gives an overview of the existing studies that focus on mixing in microscale channels and the different fouling based studies which has been used a basis to develop this work.

Chapter 3 discusses the experimental and numerical methodology employed during mixing studies, the results obtained and how the formation of Dean vortices impact mixing performance. The mixing performance has also been correlated with the strength of Dean vortices through a parameter referred to as swirling strength which can determine the strength of Dean vortices

Chapter 4 discusses the impact of geometric design on fouling resistance and how this resistance has been characterized both through numerical and experimental studies.

Chapter 5 concludes the main results obtained in this work and possible future directions for this work.

Chapter 2

Background and Literature review

2.1. Micromixers

Micromixers are generally classified into active and passive micromixers based on the force that drives mixing. Active micromixers make use of an external input energy in the form of acoustic[13], electrical[14], pneumatic[15] or magnetic energy[16] to create turbulence in the flow which would further enhance mixing, although it would be hard to integrate these mixing sections into µTAS (µ Total Analysis) systems thereby making it suitable for specific applications. Passive micromixers on the other hand make use of geometrical modifications along the channel which are also able to generate some amount of chaos in the flow without any external energy input. Some examples include lamination, sequential, chaotic flow based or through droplet generation.

Lamination flow:

In this type of mixer the different layers are separated and then rejoined with each other either in a parallel or serial manner also referred to as the split and recombination mixer as shown in Figure 2.
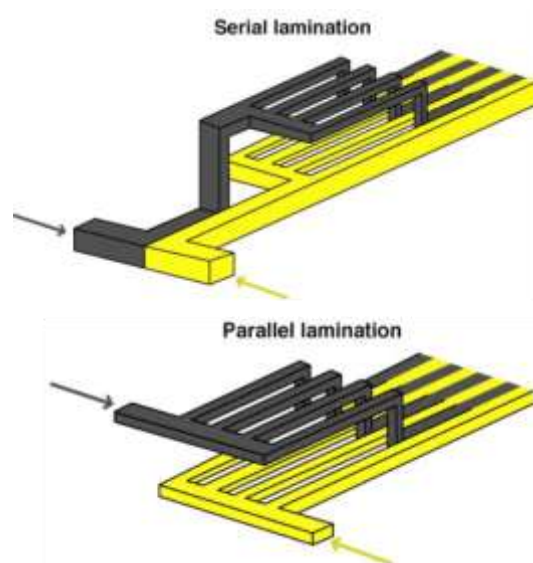
Figure 2: Illustration of serial and parallel lamination micromixers[17]

In one study Bessoth et al[18]. studied parallel lamination micromixers using 16 different branched channels on each side of a silicon wafer, joined at a central diffusive region. Both ends of the silicon wafer were closed using a glass plate to generate closed channels.
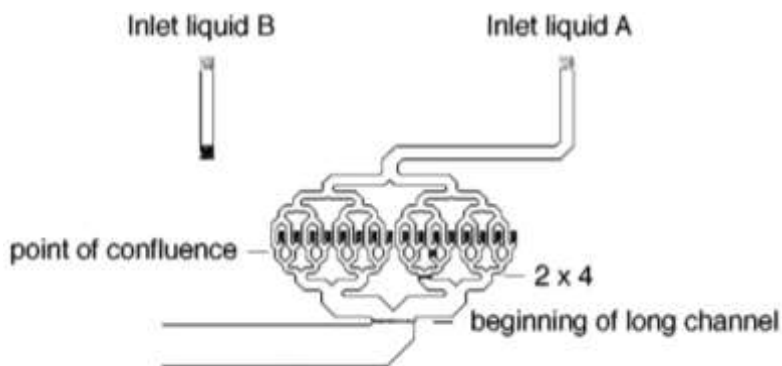
Figure 3: Illustration of lamination micromixer used by Bessoth et al. The channels have a depth of 49-58µm and a width of upto 20µm. The entire chip is 5mm x 1cm in dimension. [18]

Another study by Schönfeld et al[19] used a serial lamination design, where the channels were separated on the same plane and recombined together near the outlet. In this case, the split channels are in the same plane with minimal curvature so as to generate lamellar profiles throughout flow direction. However in several other studies the flow undergoes various disturbances due to sudden curvatures along each split before they recombine resulting in a mismatch of flow lamellae[20]. These micromixers can be used in a wide range of flow rates as demonstrated by Lee et al[21]. These lamination based micromixers are usually three dimensional in nature, thereby enhancing the rate of lamellae interaction. However they are harder to manufacture than a 2D micromixer due to alignment errors which could result in leakage. Another disadvantage of these designs would be their larger foot print area making it difficult to incorporate them within lab on a chip devices.

Figure 4: Illustration of a 3D micromixer with no obstructions along flow length[19]
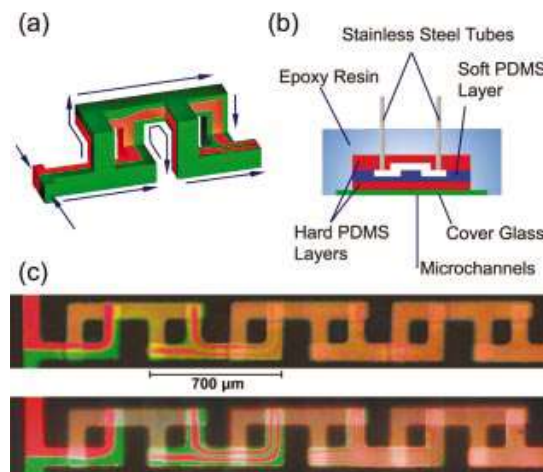
Figure 5: Illustration of 3D micromixer with serial inlet and lamination[20]

Droplet micromixer

In a study by Song et al.[22], mixing efficiency in microchannels were enhanced by manipulating the flow chemistry of liquids which would generate aqueous plugs separated by a water immiscible oil layer. This creates chaotic interaction within the plug due to fluidic stretching and folding resulting in higher mixing performance. Due to this surface chemistry manipulation these plugs can be split and mixed with each other thereby enhancing mixing between different reactants. Another work by Gunther et al.[23], use gas phase to enhance mixing between two miscible liquid streams thereby forming slug flow. This method of mixing also reports that mixing length can be reduced by 2-3 times in comparison to 3D micromixers which require complicated methods to be employed for fabrication. However on the other hand, the main disadvantage of using this method would be the usage of multi-phase fluids essential for droplet generation followed by an additional step to break these droplets to release the mixed products.

8
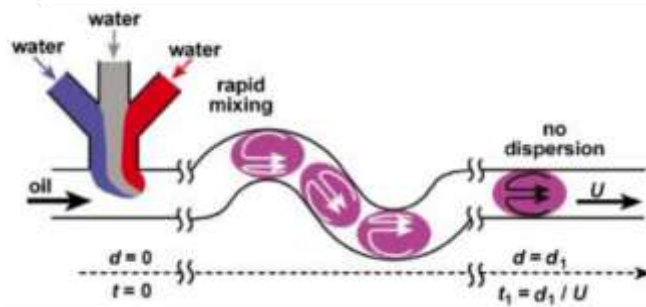
Figure 6: Droplet based mixing in PDMS based microchannels[22]

Rotation micromixer

A very common method to enhance the performance of mixing between two fluids would be through the introduction of grooves, ridges, obstructions along the channel length which in turn create vortices or induce chaos along the flow path resulting in forced interaction. Stroock et al.[24], and Liu et al.[25], have shown that the introduction of herringbone structures along the path length result in stretching and folding of the fluid causing forced interaction between the fluids at Re < 100 due to the formation of chaotic forces within the channel. While Howell et al[26], have shown that patterning herringbones on the top and bottom surface can have a more pronounced effect on mixing within these microchannels as they are able to generate vortices both in the vertical and horizontal direction which further enhances mixing and interlacing of the two fluids. Some studies have compared the performance of using a T-junction over that of a Y-junction and found that the T-junction is able to generate Dean vortices at the entrance itself which would create an impact on the mixing early on[27].
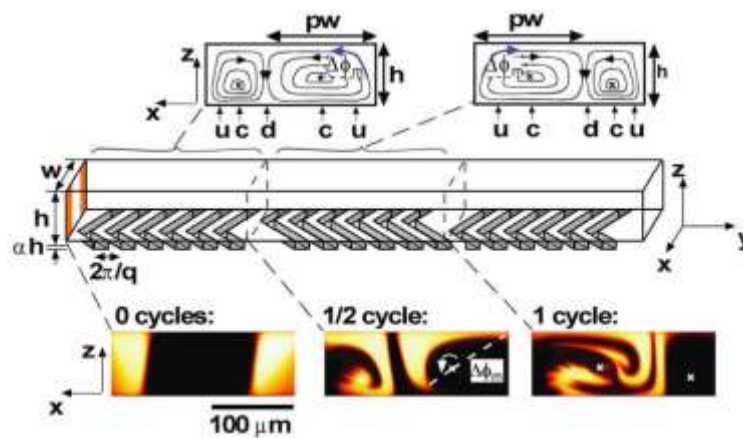
Figure 7: Introduction of vortices along the fluid path with the help of herringbone structures[24]

9

In a work by Kim et al.[28], the two mechanisms discussed earlier, splitting/recombination and stretching/folding of the fluids are combined to improve mixing through a Kendall micromixer. Flow undergoes a helical path due to the shape of the channel, while periodic barriers are placed along the fluid length to stretch and fold the fluid and they were fabricated using stereolithography.
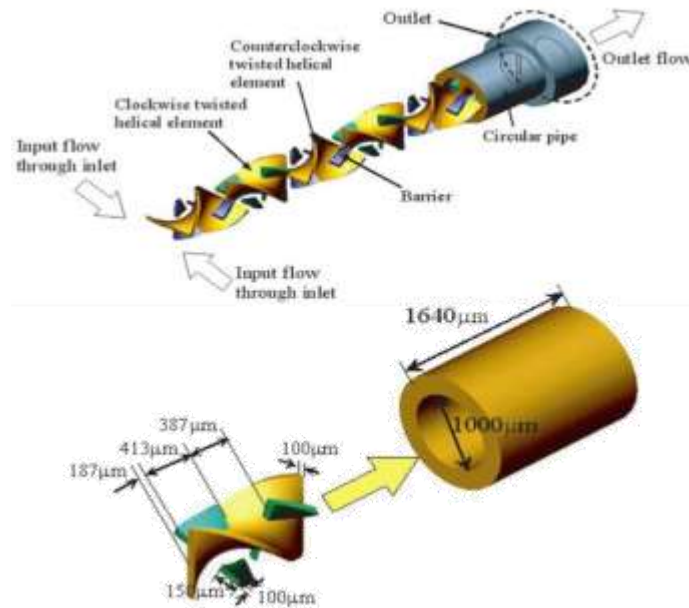
Figure 8: Barrier embedded Kendall micromixer with an alternating helical flow path that splits and recombines the fluid while the barriers stretch and fold the fluid. [28]

Some other micromixers have a 3D dimensional appearance with a straight channel in the vertical channel and curvatures which disrupt the flow boundary layer and reverse flow direction in the other plane. One such design was studied by Liu et al.[29], which shows that an improvement in mixing performance at high Reynolds number corresponds with the theory of chaotic advection showing that mixing is enhanced due to both diffusion and chaotic advection introduced due to a change in layer of mixing plane.
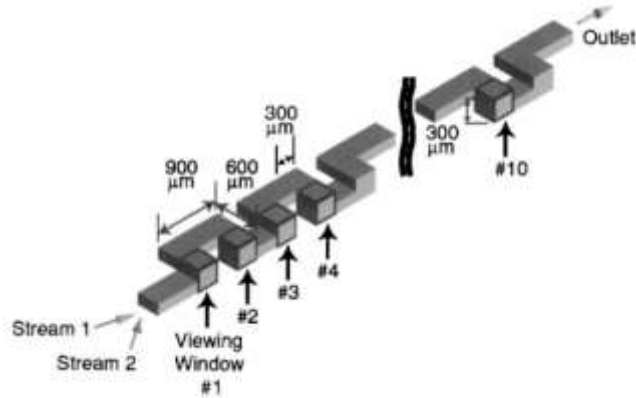
Figure 9: Three-dimensional micromixers with C shaped connectors[29]

Dean flow based micromixer

Most of the micromixers discussed have some sort of obstruction introduced along the flow path which might be difficult to manufacture. However in the case of Dean flow micromixers, introducing curvature along the channel length causes an imbalance of centrifugal forces and inertial forces which results in secondary flow in the form of vortices referred to as Dean vortices. The Dean number is represented as

$$D_e = Re\sqrt{\frac{D_h}{2R}} \ \text{.......} \ (5)$$

These Dean vortices are currently being used in various applications such as particle separation[30] and liquid purification[31]. Dean flow and associated effects in microscale mixing has been explored before by Sudarsan et al.[17], where they incorporated different in-out spiral channels in a serial manner to improve mixing performance. However they found that a spiral channel alone wasn't sufficient to produce complete mixing, thus an arc based design with lamination and bifurcation of flow or a curved channel with expansion and contraction channels were introduced so as to aid the process of Dean flow to enhance mixing performance.

A study by Scherr et al.[32], showed that by employing a S-shaped meandering curve we are able to generate Dean vortices, while reaching a mixing performance of about 86% at Re=67. While another study by Yang et al.[33], studied the effects of connecting two spirals channels one on top of the other to study the effects of a horizontal bend in between the two layers at different planes. They show that this channel between the two layers disturbs the flow profile thereby obtaining mixing performance greater than 90%.
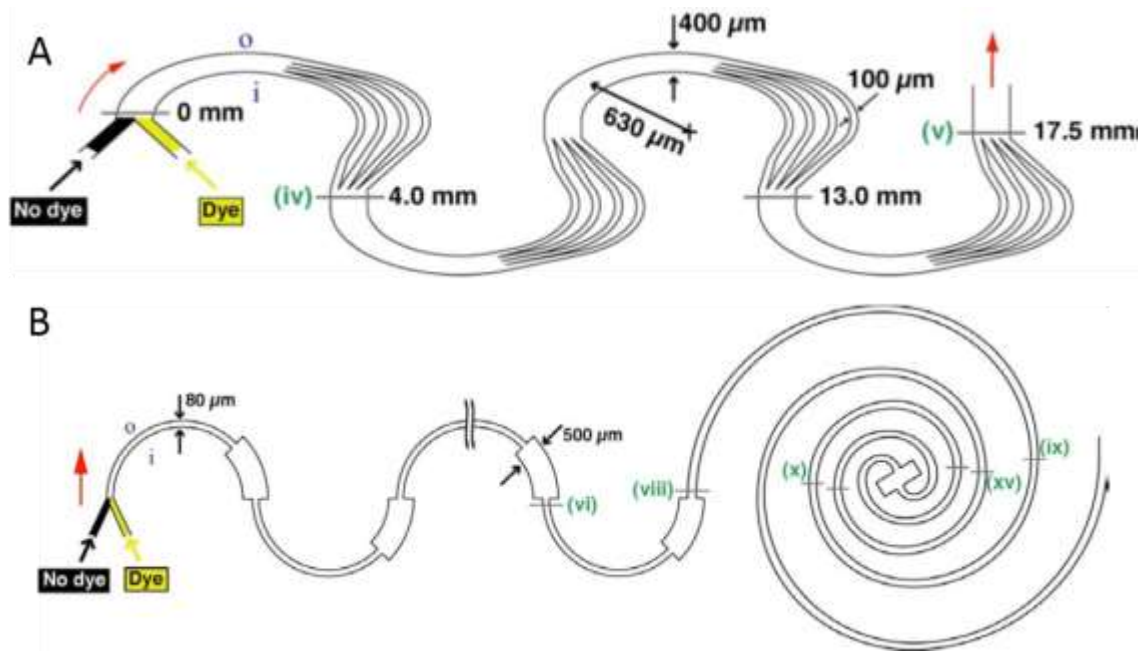
Figure 10: A) Serpentine channel with 4 split channels which are joined prior to the next turn B) Expansion and contraction channels introduced along with serpentine channels combined with a spiral channel to improve mixing performance[17].

$r_1(\theta) = -3.2e^{-0.11\theta} + 3.2$

$r_2(\theta) = -1.1e^{-0.31\theta} + 1.1$

$r_3(\theta) = -1.8e^{-0.17\theta} + 1.8$

$r_4(\theta) = -1.8e^{-0.21\theta} + 1.8$
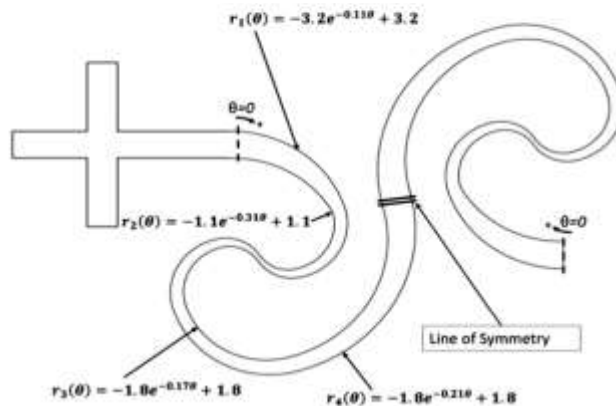
Figure 11: Logarithmic S-shaped meandering channel[32]
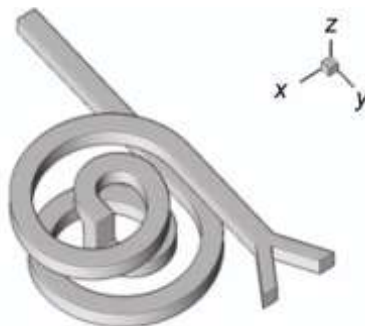
Figure 12: Spiral microchannels arranged in a parallel manner connected by a vertical connecting channel[33].

On the other hand, helical flow has been generated through fabricating complicated structures as shown in Figure 13 which was fabricated using stereolithography. They were shown to improve mixing considerably within very small pressure drops along the flow length.
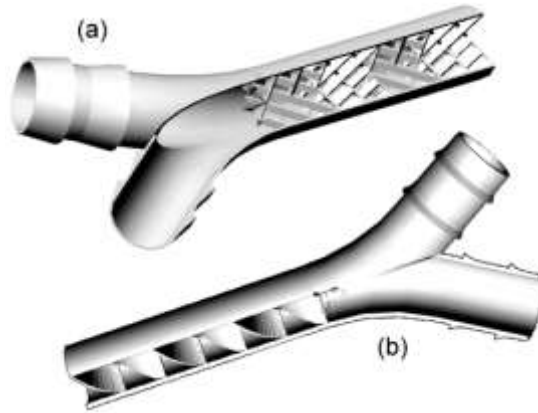
Figure 13: Ceramic based helical micromixer designs[34]

This work would be focusing on enhancing mixing performance due to the formation of Dean vortices in a channel by using a passive method of continuous spiral channel since diffusion is a very long process which would require longer length of the channel while convective forces in the form of Dean flow could further enhance this process. This study will be using channels with dimensions in the larger microscale range while studying flow interaction at higher flow rates thereby reducing mixing time and pumping power required for flow. The use of this spiral design also ensures that the total footprint area occupied by the channel is reduced while enhancing mixing due to turbulence induced by the secondary flow.

2.2. Fouling based studies

Fouling is found to be a major issue in various microscale devices used for heat based studies and those employed in various chemical engineering applications.

Epstein (1983)[35] classified fouling into five primary categories based on the physical and chemical processes that drive fouling as:

1. Crystallization fouling: This class of fouling is further divided into two sub classes:

a. Precipitation fouling: This occurs in systems which use dissolved salts that crystallize onto the heat transfer surface also referred to as scaling. Most salts precipitate on subcooled surfaces, however certain salts like calcium sulphate precipitate on superheated surfaces as they are less soluble in warm streams.

b. Solidification fouling: When a pure liquid is frozen to ice or when low melting components of a multi component solution freeze onto a sub cooled surface it is referred to as solidification fouling as they are formed through the crystallization of fluid.

2. Particulate fouling

Fine particles dissolved in the working fluid can get deposited onto the heat transfer surface. Many a times due to their concentration, these particles settle down under gravity and can be referred to as sedimentation.

3. Chemical reaction fouling

The by-products of a chemical reaction might be deposited on the exchanger surface due to their difference in chemical properties such as density, solubility to name a few. In such cases the material surface might have to be modified to prevent them from being destroyed under the effect of these chemical reactions.

4. Corrosion fouling

This is the most destructive form of fouling as it results in reduction in material surface available for heat transfer. The accumulation of corrosive by products of working fluids can result in erosion of the material surface.

5. Biological growth fouling

Adhesion of biological matter present in the fluid is referred to as biological growth fouling. Deposition of such matter can alter the physical properties of the adherent surface as well the flow properties due to the slimy nature of the biological matter on the surface.

Although these are the five different types of fouling, the events in the process of fouling are:

1. Initiation: This refers to the delay period experienced between the start of flow and any amount of appreciable fouling for a clean heat transfer surface. For crystallization fouling this depends on crystal nucleation process which affects the delay period that onsets initiation. However for a chemical reaction fouling, the delay period decreases as the surface temperature increases. Surface roughness can also affect the delay rate due to entrapment of bubbles, eddies and flow along the heated surface. While in the case of biofouling, adsorption of glycoproteins onto the heated surface due to their presence in natural water, provide micro-organisms a suitable platform for attachment[36].

2. Transport: This is one of the critical steps during fouling and the rate of transportation of dissolved particles depends on the transport coefficient of these particles, concentration of the primary fluid and dissolved particles. Based on particle density the transportation of loaded particles on to the surface can also be mediated by gravity while the temperature of the wall surface can also influence transportation as cold surfaces attract colloidal particles while hot surfaces repel colloidal particles.
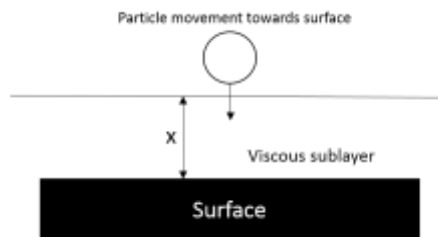
Figure 14: Illustration particle movement over a surface

As a particle moves along with the bulk fluid its movement towards the wall surface is assumed to be at right angles. Just above the wall surface up until a distance of x, the flow generates a viscous sub layer and once the particles obtain sufficient energy to cross this barrier, deposition of particles take place as illustrated in Figure 14. For a particle undergoing Stoke's drag, the particle relaxation time is represented as:

$$t_r = \frac{\rho_p d_p}{18\mu_f}$$

where ρ_p and d_p represent the density and diameter of the particle respectively while μ_f represents the viscosity of bulk fluid. This is the time taken by the particle to move through distance x at an initial velocity v.
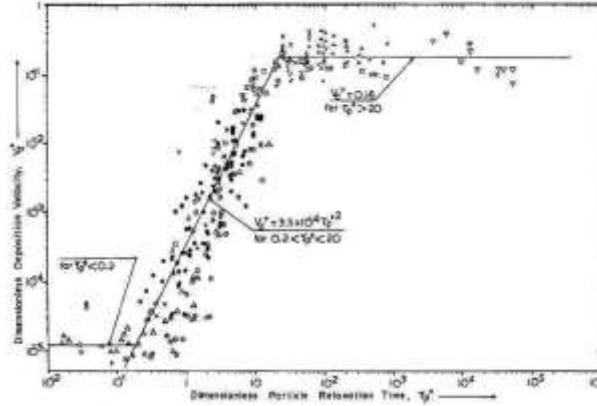
Figure 15: Illustration of a plot showing the variation between deposition velocity and time[37]

The dimensionless relaxation time and velocity is given as:

$$V^* = V_f \sqrt{\frac{f}{2}}$$

$$t_r^+ = \frac{t_r(V^*)^2}{\nu}$$

$$k_m^+ = \frac{k_m}{V^*}$$

where f is the fanning friction factor, V* and V_f the friction and fluid velocity respectively, while v is the kinematic viscosity. Based on t_r^+ and k_m^+ plots, the transport regime is divided into three regimes as below. However only the diffusion transport occurs in laminar flow regime while the other two fall into the turbulent regime.

3. Diffusion particle transport

Diffusion of particles are determined through Brownian motion of the fluid molecules and these loaded particles. The particle diffusion coefficient is determined through the Stokes-Einstein equation as

$$D = \frac{kT}{3\pi\mu_f d_p}$$

16

where k is the Boltzmann constant (1.38 x 10^{-23}J/°K), T the absolute temperature of the fluid, and d$_p$ the particle diameter. Smaller particle size promotes greater diffusion of particles which in turn promotes deposition of particles, while increased temperature has the same effect on particle deposition due to increased diffusivity term and reduced fluid viscosity at higher temperature. The deposition rate of particles are determined through the Sherwood number represented as below[38]:

$$Sh = \frac{kD_h}{D} = \frac{Mass\ transfer\ rate}{Diffusion\ rate}$$

Where k is the mass transfer coefficient and in this experimental work it is taken as the change in number of particles at different time points

$$k = \frac{N(t + \Delta t) - N(t)}{Ac\Delta t}$$

where N is the number of particles at a given time, A the area of interest, and c the concentration of the bulk fluid introduced in the study.

In another study by Masri and Cliffe, they developed a correlation for plate fin minichannel heat exchanger. They estimate the particle mass transfer coefficient as

$$Sh = 0.664Re^{0.5}Sc^{0.33}$$

$$Re = \frac{\rho V_f D_h}{\mu}$$

$$Schmidt\ number = Sc = \frac{\mu}{\rho D}$$

4. Inertial particle transport

In this regime the particles would have obtained sufficient energy to cross the viscous sub layer. Once they cross the sub layer they move under Brownian motion and those with sufficient energy reach the wall surface. This regime was numerically represented by Papavergos and Hedley[37] as:

$$k_m^+ = 3.5\ x\ 10^{-4}(t_r^+)^2$$

4.1. Impaction particle transport

In this regime the particle attains the friction velocity V* as it moves towards the wall. Papavergos and Hedley[37] estimated $k_m^+ = 0.18$ in this regime.

5. Attachment: Once the particles are transported on to the wall surface, their attachment depends on competing forces as illustrated in Figure 16.
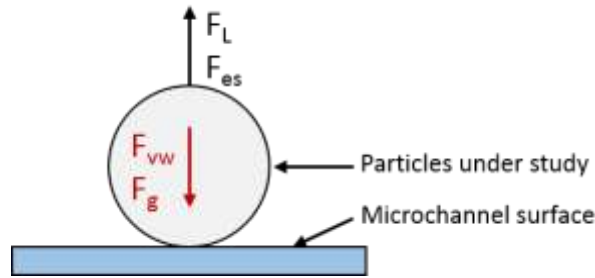
Figure 16: Illustration of forces acting on a particle during flow through a microchannel

5.1. Gravity force

Gravity is a key force which drives particles towards the wall during horizontal flow making it an adhesive force. Gravitational force of a particle in water is given as:

$$F_g = \frac{\pi d_p^3(\rho_p - \rho_f)g}{6} \quad \ldots\ldots\ldots\ldots (6)$$

Where d_p is the particle diameter, ρ_p and ρ_f the density of particle and fluid respectively. However, in this study the particles are in the range of nanometer scale, thus their effect is negligible however they would have a greater impact if they aggregate, which is avoided before flow is introduced.

5.2. Van der waal's force:

Van der Waal's forces are attractive forces between atoms or non-polar molecules due to dipoles generated. Van der waal's force between a moving particle and wall along with retardation forces can be represented as:

$$F_{vw} = \frac{A_{132}d_p}{12H^2}\left[1 - \frac{1}{1+\frac{\lambda_c}{5.32H}}\right], H \ll \frac{d_p}{2} \quad \ldots\ldots\ldots (7)$$

18

Where A_{132} is the Hamaker constant of particle 1 in medium 3 while interacting with wall 2, d_p the particle diameter, H the minimum separation between wall and particle, λ_c the London characteristic wavelength taken to be 100nm[39,40]. The van der Waal's forces between two particles are usually in the range 10^{-19}- 10^{-20}J, however the presence of a secondary medium of dispersion retards particle flow causing the van der Waal's force to reduce. Thus the Hamaker constant for the particles can be calculated as[41]

$$A_{132} = (\sqrt{A_{11}} - \sqrt{A_{33}})(\sqrt{A_{22}} - \sqrt{A_{33}})$$

where A_{11}= 7.9 x 10^{-20}J (Polystyrene), A_{22}= 4.4 x 10^{-20}J (PDMS) and A_{33}= 3.7 x 10^{-20}J (water), thus A_{132}=1.5 x 10^{-21}J.

5.3. Electrostatic force

Liquid surface may be charged due to the dissociation of surface groups such as silanols and ions or through the adsorption of molecules from the surroundings. So as to maintain charge neutrality in the system, the fluid may contain charges of the opposite signs, resulting in an unequal charge distribution of ions at the surface and rest of the fluid. Thus the region near the surface is referred to as the electric double layer (EDL) and this region can be further sub divided as Stern layer and diffuse layer. Immobile layer of ions with strong bonds near the wall surface are referred to as the Stern layer. While the layer just beside this layer is referred to as the diffuse layer with loosely moving ions. This EDL formation also minimizes the Gibbs free energy of the solution.
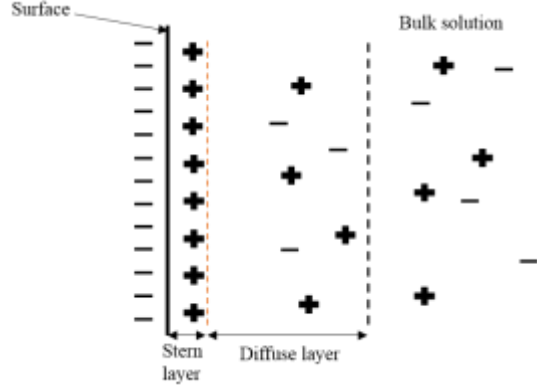
Figure 17: Different layers of electrostatic force during flow over a flat surface

For monovalent ionic solutions such as NaCl, the Debye Huckel parameter and surface potential are defined as:

$$\kappa = \sqrt{\frac{2z^2 e^2 C_0}{\varepsilon k_B T}}$$

$$\Psi = \Psi_s e^{-\kappa x}$$

This parameter determines the thickness of the diffusion layer in the solution as determined by $1/\kappa$ also known as the Debye length and at this distance of $1/\kappa$ the potential falls to a value $1/e$ of the surface potential. This region is usually a part of the diffuse layer[56].

Several studies have been conducted to derive the electric double layer force, however no standard form has been developed as most works debate on which parameters are to be kept constant while obtaining this force. In this work the surface potentials are assumed to be constant due to the microscale and relative uniformity of the solution. Electric double layer force is estimated to be

$$F_{EDL} = \frac{4\pi \varepsilon_o \varepsilon d_p \zeta_p \zeta_w \tau}{2kT_o} \left[\frac{e^{-\tau H}}{1+e^{-\tau H}} - \frac{(\zeta_p - \zeta_w)^2}{2\zeta_p \zeta_w} * \frac{e^{-2\tau H}}{1-e^{-2\tau H}} \right] \quad .....(8)$$

where ζ_p and ζ_w are the zeta potential of the particle and channel wall respectively, d_p the particle diameter, τ the ratio of particle radius ($\frac{d_p}{2}$) and Debye length (κ^{-1}), ε_o and ε permittivity of vacuum and relative permittivity of water,

5.4. Hydrodynamic force

The lift force experienced by a particle in contact with a fixed wall under shear flow was formulated by Leighton and Acrovis (1985)[42] as:

$$F_L = 0.58\rho_f \left(\frac{\tau_w}{\mu_f}\right)^2 d_p^4 \quad \ldots\ldots\ldots (9)$$

$$R_{ep} = \frac{\rho v_p d_p}{\mu}$$

Where ρ_f and μ_f is density and viscosity of bulk fluid, τ_w shear stress of the wall, d_p the particle diameter and v_p the particle velocity at a distance $y = \frac{d_p}{2}$. However this expression is only valid for $Re_p < 1$. Shear stress of fluid along the wall can be calculated as the gradient of fluid velocity as:

$$\tau_w = \mu_f \left(\frac{du}{dz}\right)$$

Where $\left(\frac{du}{dz}\right)$ is the shear rate or velocity gradient at the wall. The drag force on the particles are defined as:

$$F_D = 1.7 * 3\pi\mu_f d_p v \quad \ldots\ldots\ldots (10)$$

In addition the surface roughness can also affect the drag force experienced by the particles as particles can get trapped in these roughness, and as a result the shear stress required to prevent deposition also increases.

For ionic particles, the sign of zeta potential between the particle and wall surface determines the nature of force. Zeta potentials of opposite signs ensure that electric double layer attractive forces would add to the attractive Van der Waal's force resulting in mass controlled deposition of particles. However as particles get deposited onto the wall surface zeta potential of the surface is altered causing it to change sign, resulting in electric double layer forces that are repulsive in nature. This

repulsive force in combination with Van der Waal's attractive force can prevent further deposition of particles. Hence one way to minimize the rate of fouling or deposition is to adjust the zeta potential of the working fluid. However for products of chemical reaction, the rate of deposition is dependent on the Arrhenius equation that control reaction kinetics.
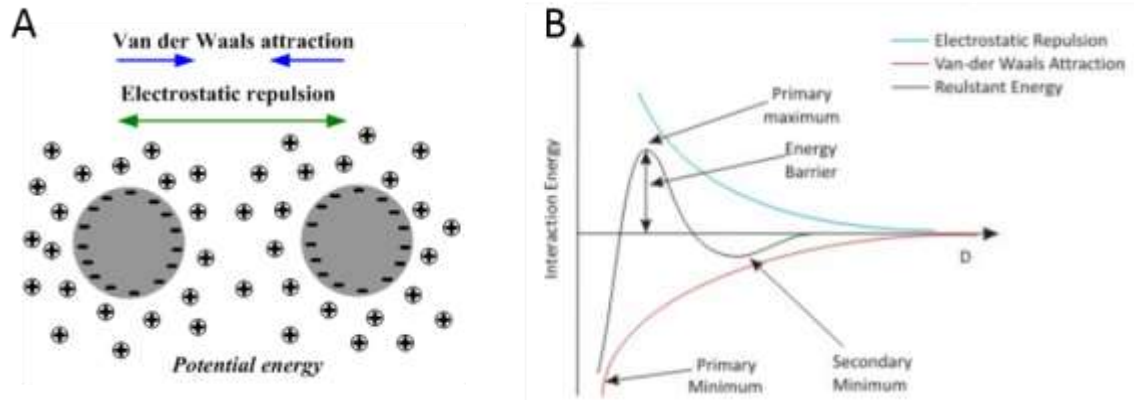
Figure 18: Illustration of Van der Waal's forces[57]

6. Removal: This doesn't come into play until the particles have been deposited and the removal rate is dependent on the thickness of deposition which indirectly varies with the rate of mass flux deposition[43].

7. Aging: Aging of the accumulated particles begin upon their deposition and various changes can occur to these particles in the form of drying, polymerization, oxidation etc:- In addition, the deposition can reduce over time due to chemical or physical breakdown of these particles thereby removing particles that can't be removed hydrodynamically.

The different methods of fouling and the steps towards fouling is typically described as a 5x5 matrix as shown in Figure 19.

	1. Crystallization fouling	2. Particulate fouling	3. Chemical reaction fouling	4. Corrosion fouling	5. Biological growth fouling
1. Initiation	1.1	1.2	1.3	1.4	1.5
2. Transport	2.1	2.2	2.3	2.4	2.5
3. Attachment	3.1	3.2	3.3	3.4	3.5
4. Removal	4.1	4.2	4.3	4.4	4.5
5. Aging	5.1	5.2	5.3	5.4	5.5

Figure 19: Classification of fouling regimes[44]

In heat exchangers, the rate of fouling can be quantified using two basic parameters: pressure drop and fouling resistance as fouling is dependent on temperature and flow velocity. Buildup of particles over time results in reduced flow path, resulting in higher pressure drop along the channel length.

The fouling resistance of macro scale heat exchangers are calculated by taking into consideration mass deposition and heat transfer effectiveness at time t-t_0 when flow is just introduced and t=t_1 when considerable amount of deposition has occurred which causes the thickness of the wall to increase thereby reducing the amount of heat transferred. For a given heat flux applied on the walls at $\dot{q}$, where the temperature of the bulk fluid is T while the wall temperature is T_w, the thermal resistance prior to the initiation of fouling is represented as [45]

$$\frac{1}{U_0} = \frac{T_{w0} - T}{\dot{q}}$$

While the thermal resistance after time 't' is represented as

$$\frac{1}{U} = \frac{T_w - T}{\dot{q}}$$

The difference in thermal resistance can be represented as the fouling resistance R_f

$$R_f = \frac{1}{U} - \frac{1}{U_0} = \frac{T_w - T_{w0}}{\dot{q}}$$

showing that fouling is a time dependent process.

While the mass deposition rate on the wall is represented as $m = \frac{\rho_f \, dx_f}{dt}$

$$\frac{dm}{dt} = \phi_D - \phi_R$$

Where ϕ_D and ϕ_R are the mass deposition and removal rates per unit area respectively. The fouling resistance can also be written in terms of the layer thickness and its density as $R_f = \frac{x_f}{\rho_{fouling}}$

$$m = \frac{\rho_f \cdot \rho_{fouling} \cdot (T_w - T_{w0})}{\dot{q} \cdot t}$$

Fouling models:

Fouling in these microchannels can be modelled as described below and each of them are subject to a delay or induction period in the start as described earlier:

1. Linear model

Ignoring the initial delay, fouling resistance in the linear model can be expressed as $R_f = a.(t - t_0)$, where t_0 is the time after initiation has been completed and a, the slope of this curve represented as the change in fouling resistance or the time differential of fouling resistance $\frac{\partial R_f}{\partial t}$. This slope is also dependent on the difference in deposition and removal rate of particles where the removal rates are lower due to strong bonds between the deposited particles and surface thereby resulting in a continuous increase in the rate of deposition and fouling resistance.

2. Asymptotic model

This model is commonly seen in cooling water heat exchangers. This model was mathematically represented by Kern and Seaton[46] as:

$$R_{ft} = R_{f\infty}(1 - e^{-\beta t})$$

where $R_{f\infty}$ is the fouling resistance at infinite time, while β is characteristic of the system and operating properties while the mass deposited per unit area at a given time 't' is represented as:

$$M = M^*(1 - e^{-\beta t})$$

where M^* is the mass deposited per unit area at infinite time. From the above two equations we can derive that at a given time t,

$$R_{tf} = \frac{M}{\rho_f k_f}$$

where ρ_f and k_f are the density and thermal conductivity of the foulant. Their work also shows that

$$M^* = \frac{a_1 C_b V_m}{a_2 \tau_w}$$

$$\beta = a_2 \tau_w$$

Where a_1 and a_2 constants dependent on the system, C_b the bulk concentration of the fouling material, V_m mean fluid velocity and τ_w wall shear stress.

$$\frac{dM}{dt} = \phi_D - \phi_R$$

Based on these equations the deposition and removal mass fluxes can be defined as:

$$\phi_D = a_1 C_b V_m$$

$$\phi_R = a_2 \tau_w M$$

3. Falling rate model

   This model describes those cases whereby deposition of particles do not reach an asymptotic value neither does it increase linearly as it increases in a non-linear manner. Over time the difference in deposition and removal rate gradually decreases resulting in this non-linearity. This variation can be attributed to the fact that the process might not have been run long enough for it reach an asymptotic value of fouling.
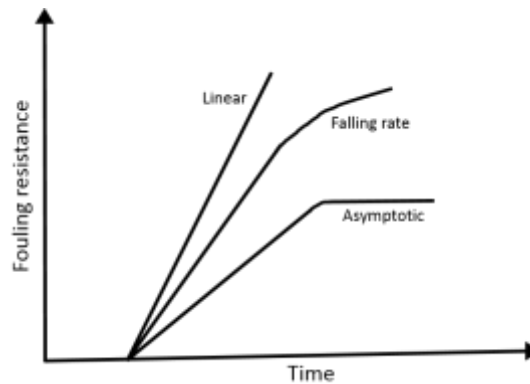
Figure 20: Different models of fouling

25

Chapter 3

Mixing of fluids in microchannels

This chapter elaborates the various designs implemented to study mixing in microchannels and the advantages of using certain designs.

3.1. Materials and Methods

3.1.1. Design and fabrication of the microfluidic device

Since studies were conducted on PDMS based microfluidic devices, a mold/ template needs to be developed so that PDMS molds can be casted from this using soft lithography. Usually these molds are developed using a time consuming photolithography procedure which involves a silicon substrate, a template mask and various etching chemicals as described in Figure 21. In this study the mold was fabricated using 3D printing (stereolithography) (ProtoLabs Inc., USA)
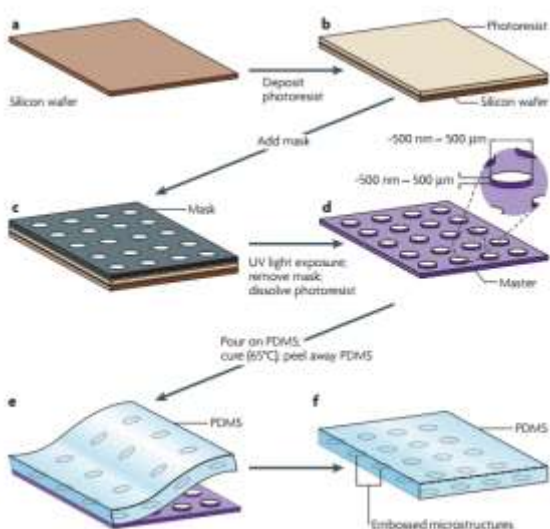
Figure 21: Illustration of microfabrication using photolithography[1]

Stereolithography uses an ultraviolet laser light to draw on the surface of a liquid thermoset resin by focusing it to a small point thereby solidifying the liquid polymer. This is then repeated in a layer by layer manner along the 2D plane to generate 3D structures. The overall time taken for 3D printing such microscale molds can vary from a few minutes to a few hours based on the precision level required. Prior to printing the 3D structure, support structures are developed to prevent the design from collapsing. In order to ensure that each layer is built to precision, visual inspection through imaging is employed. Upon completion of the print, the external and interior support structures are removed using suitable solvents. In order to maintain a superior surface finish the surface is sand down using a sand paper to remove any

remnant support structures. The material SL Accura 5530, which is made of 10% glass reinforced polycarbonate was chosen owing to its high temperature resistance which enables us to cure it at high temperatures during soft lithography. Having fabricated the mold, PDMS replicates of these designs were fabricated by a process called soft lithography[1]. PDMS Sylgard 184 (Dow Corning) and curing agent are mixed in the ratio 10:1 and degassed in a vacuum desiccator for 45mins-1 hour, following which it is cured overnight at 60˚C. The PDMS replicates are peeled off the mold, and holes with a diameter of 1.5mm are punched onto the PDMS substrate using a Biopsy puncher. The PDMS devices are then bonded to a sheet of glass through plasma activation. Upon bonding the fabricated device is left in an oven at 80˚C for 1 hour to ensure strong bonding between the PDMS device and glass substrate. Various designs were fabricated for this study and they were modeled using Solidworks 2015 and sent for stereolithography/ 3D printing. The molds fabricated by this method are then spray coated with a layer of adhesive to ensure easy removal of PDMS upon casting. Through this study we aim to understand the effect of curvature and thus various designs namely a curved spiral with varying cross sectional profile, serpentine, saw tooth, U-shaped, and a simple curved channels were used. In addition the cross sectional profile of the spiral channel was varied to understand the effect of varying cross sectional profile (rectangular, square, semi-circle, and trapezoid) on the effect and strength of secondary flow developed within the microchannels. The different designs studied are illustrated in Figure 22.
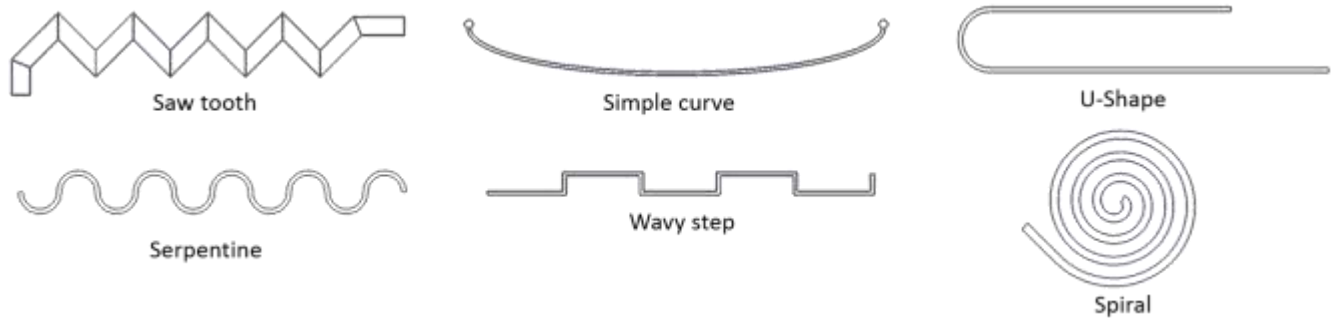
Figure 22: Illustration of the different curvature designs used in this study

While varying the cross sectional profile of the spiral channel, the cross-sectional area was to be kept constant at 0.36mm^2. The dimensions of the various cross sectional geometries chosen are illustrated in Figure 23 and Table 1. The spiral channel was modelled as a logarithmic spiral with 3.5 turns with an initial

angle of 100 degree at the center giving it a total length of 76.76mm with 2 inlets which meet each other at a Y-junction. An additional straight section is added to the channel so that the flow is fully developed prior to entering the spiral section thereby giving a total fluidic length of 87.73mm. The substrate roughness of the PDMS substrate obtained using a 3D printed mold and an aluminium substrate are illustrated in Table 2. It was found that their surface roughness are comparable making this method of mold fabrication a suitable alternative to expensive milling or photolithography.
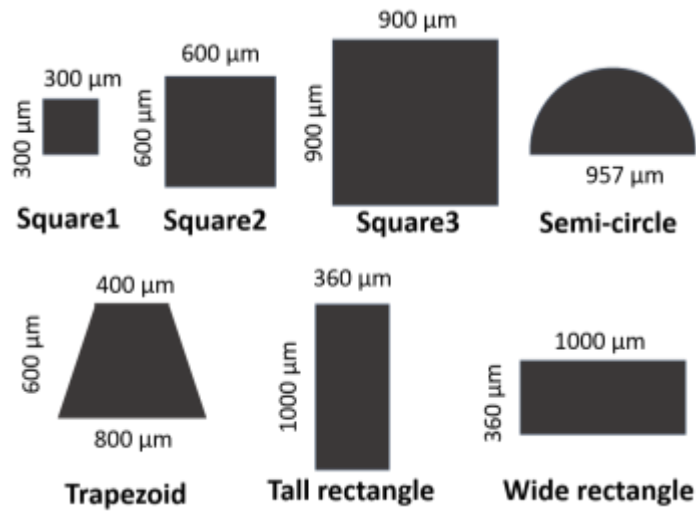
Figure 23: Illustration of the different cross sectional geometries studied for a spiral microchannel

Table 1: Dimensions of all the spiral channels used in this study

Shape	side a (top side) (µm)	side a1 (bottom side) (µm)	side b (height) (µm)	Dh(µm)	Area (µm²)
Square 1	300	-	300	300	90000
Square 2	600	-	600	600	360000
Square 3	900	-	900	900	810000
Tall rectangle	360	-	1000	529.4	360000
Wide rectangle	1000	-	360	529.4	360000
Trapezoid	400	800	600	584.2	360000
Semicircle	957 (diameter)	-	-	585	360000

Table 2: Surface roughness of PDMS substrates obtained using the 3D printer polymer mold and aluminium based mold

	Polymer-based molds	Aluminum-based molds
Surface Roughness (nm)	300	250

3.1.2. Numerical studies

Flow visualization and shear flow studies were conducted using a commercial CFD package (Ansys Workbench 15). The design modeled using Solidworks was imported into the inbuilt workbench design modeler, and meshed using the inbuilt meshing tool thereby dividing the computational grid into elements of size 30-50µm generating between 500,000 to 1.5 million nodes depending on the complexity of the geometry. The software uses Navier-Stokes continuity and convection-diffusion equations by assuming a Newtonian laminar flow along the microchannel length represented in equations 11-13.

$$\frac{\partial V}{\partial t} + V.\nabla V = -\frac{1}{\rho}\nabla P + \frac{\mu}{\rho}\nabla^2 V \ldots\ldots\ldots\ldots (11)$$

$$\nabla.V = 0 \ldots\ldots\ldots\ldots (12)$$

$$\frac{\partial c}{\partial t} + (V.\nabla)c = D\nabla^2 c \ldots\ldots\ldots\ldots (13)$$

where V is the velocity vector, µ dynamic viscosity, ρ fluid density, P pressure, c concentration of fluids, and D the diffusion coefficient. The ideal grid size was obtained by conducting a mesh dependency study so that the pressure drop along the channel length did not vary much with varying grid size while being able to solve the model in finite time. In order to speed up the computational process irregular geometries such as the semi-circular and trapezoidal profiles were sliced along a particular plane so as to enable parallel meshing and solution of the geometry. One set of data obtained through this mesh dependency study for a spiral channel with a square cross section of 600µm is illustrated in Table 3. In this case, the intermediate mesh size of 3e-5 was shown as an ideal mesh by taking into consideration computational time and percentage change in pressure drop obtained from inlet to outlet.

Two fluids (water) were then introduced through the two inlets to the different channel designs at varying volumetric flow rates of 270µl/min, 540µl/min and 800µl/min at each inlet which corresponds to a flow

velocity of 0.025m/s, 0.05m/s and 0.074074m/s for all geometries with a cross sectional area of 0.36mm^2. The density and viscosity of water chosen was 998.2 kg/m^3 and 0.001003 kg/m-s respectively whilst the diffusion coefficient was set to be 2.3 x 10^{-9} m^2/s. By varying the flow velocity the impact of mixing with varying Reynolds number can be studied as the Dean number is represented by the equation:

$$D_e = R_e \sqrt{\frac{D_h}{2R}}$$

where R_e is the flow Reynolds number, D_h the hydraulic diameter and R the average radius of curvature of the spiral channel. Reynolds number in turn improves the Dean number which impacts the interaction between two fluids thereby improving the rate of mixing.

Table 3: Grid dependency study conducted for a spiral channel with a square cross section of hydraulic diameter 600μm

Size	No of elements	dP (Pa)	Percentage change (%)
2.50E-05	1779936	412.61	2.64
3.00E-05	1027640	401.73	2.88
3.50E-05	652443	390.16	1.36
4.00E-05	434190	384.86	1.24
4.50E-05	311558	380.07	1.63
5.00E-05	223800	373.87	---

The solutions were set to be converged if the residual values drop to under 10^{-6} for continuity and velocities. The mass fraction of stream 1 and 2 species at inlet 1 were specified to be 1 and 0 respectively, and at inlet 2 the mass fraction of stream 1 and 2 were specified to be 0 and 1 respectively while the mass fraction at the outlet were set to 0.5 for both streams since equal volumes of stream 1 and 2 are introduced at the inlet. From these simulations swirling strength and mixing performance were obtained at various positions along the spiral length. Swirling strength provides information about the ratio of tangential velocity and core velocity, which acts as an indicator of the vortex strength and the area average value of swirling strength at the outlet was obtained for each of the geometries under study. The mixing performance of the fluids was

determined by taking into consideration the mass flux of both streams at the outlet and represented by the equation:

$$\sigma = \sqrt{\frac{1}{n}\sum_{i=1}^{n}(m_i - \bar{m})^2}$$

Where m_i is the mass flux at a given point, $\bar{m}$ the average mass flux at the outlet, n the number of points taken into consideration in this analysis and σ the standard deviation of mass flux. The number of points considered in each case depends on the number of mesh elements. The mixing performance is then represented as:

$$MP = 100 * (1 - \frac{\sigma}{\sigma_{max}})$$

where σ_{max} is the maximum attainable mixing index (0.5). The highest possible value of σ is 0.5 since the maximum possible value of each stream at the outlet is 0.5 since equal amounts of each stream were introduced through inlet 1 and 2. In this way a 100% mixing would indicate complete mixing while 0% would indicate no mixing at all.

Solidworks design   Design after meshing   Volume rendering of mass fraction of fluid 1 along the channel length

Figure 24: Illustration of the spiral design, after meshing and mass fraction of the fluid after the simulation has been completed

3.1.3. Mixing experiments and visualization:

PDMS channels were first fabricated for each of the above mentioned designs and bond to a glass bottom surface. Tygon tubing (Cole Parmer, US) was connected to the fluidic access holes to facilitate fluid flow to the microfluidic channels through a fluid control system. In order to visualize the phenomenon of fluid

mixing due to formation of Dean vortices, cross-sectional time-lapse images of two streams of de-ionized (DI) water were obtained using a laser scanning confocal microscope (Olympus) with a 10x objective of resolution 2048 x 2048 pixels. Of the two streams of DI water introduced at the inlet, one stream was tagged with 10 µM of fluorescein dye (Sigma Aldrich) while the other stream was pure DI water. Flow was introduced into these microchannels using a high-accuracy syringe pump (PHD 2000, Harvard Apparatus) at a constant volume flow rate ranging from 0.1 µl/min to 4000 µl/min through each inlet as illustrated in Figure 25. The mixing index represented by the standard deviation of intensity values was then characterized in ImageJ using the formula $\sigma = \sqrt{\frac{1}{n}\sum_{i=1}^{n}(I_i - \bar{I})^2}$, where I_i is the intensity value at a given point and $\bar{I}$ is the mean intensity value for the given cross-section measured in W/m^2. A σ of 0.5 indicates no mixing while a σ of 0 indicates complete mixing. In order to obtain the level of mixing as a performance, the mixing index was modified as:

$$MP = 100 * (1 - \frac{\sigma}{\sigma_{max}})$$

where σ_{max} is the maximum attainable mixing index (0.5). In this way a 100% mixing would indicate complete mixing while 0% would indicate no mixing. Z-stack images were obtained at every 90° turn from the inlet to outlet so that the improvement of mixing with varying radius of curvature can be studied.
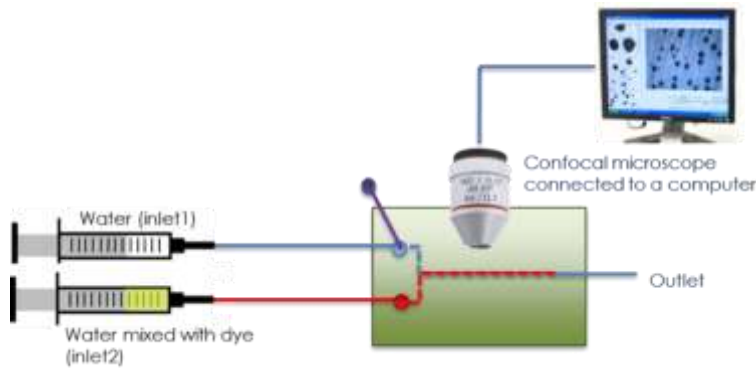
Figure 25: Illustration of the experimental set up for micromixing study

3.2. Visualization of Dean vortices and flow field in the microchannels

In order to understand the nature of flow field inside the microchannels, a fluorescent dye was injected into the microchannels at varying flow rates as described in the above section and visualized using confocal microscopy. Figure 26 illustrates the flow field in the different curvature designs namely serpentine, saw tooth, spiral, square curve and u shape with a square cross-sectional profile at a volumetric flow rate of 800µl/min (Re=45) taken at the outlet. These images demonstrate that the microchannels are able to disturb flow field along its axial direction of flow while the spiral channel is able to generate Dean vortices characterized through the presence of distinct counter rotating vortices. Figure 27, illustrates the formation of Dean vortices (two counter-rotating vortices) which are generated due to an imbalance of curvature induced centrifugal force and flow velocity.
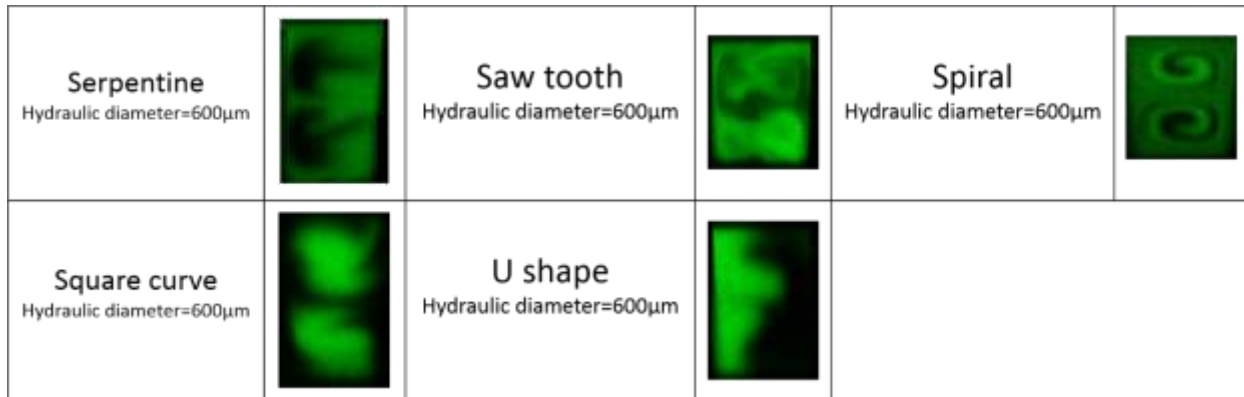
Figure 26: Illustration of flow field in the different curvature designs at a volumetric flow rate of 800µl/min (Re=45) taken at the outlet.

Apart from observing flow field in the previous mentioned curvature designs, spiral channels of varying cross-sectional geometries (square, rectangular, semi-circular and trapezoidal), and hydraulic diameters were studied to understand their impact on the strength of secondary flow Dean vortices and mixing performance. The evolution of secondary flow in the form of Dean vortices is visualized through confocal microscopy (Figure 28 left) and numerical simulation (Figure 28 right) along the length of square channel with a hydraulic diameter of 600µm at a Reynolds number (Re) of 30. From Figure 28, it can be inferred that although the two fluids enter the channel in the longitudinal direction, secondary flow along the channel is generated in the transverse plane which pulls one fluid into the other fluid, thereby disrupting the

boundary between the two streams as illustrated in Figure 27. This recirculating flow occurs in the curved channel via the formation of Dean vortices which is initiated at a Dean number greater than 10, which is reached approximately upon the fluid entering the second loop of the spiral channel design (i.e. Figure 28e onwards) at this Reynolds number (Re=30). In the present channel design, flow travels inward from a higher radius of curvature to a lower radius of curvature, thereby strengthening the effect of the Dean vortices due to an increase in the Dean number along the microchannel length. This also gives us insight into how Dean vortices evolve into fully developed stable vortices along diverse radii of curvature, enabling us to attune Dean vortices to maximize mixing performance through design modifications. The initiation of Dean vortices does not mean that they aid the process of mixing since they need to obtain sufficient strength before they can influence the process of mixing, thus understanding the strength of Dean vortices within microchannels would be of great use.
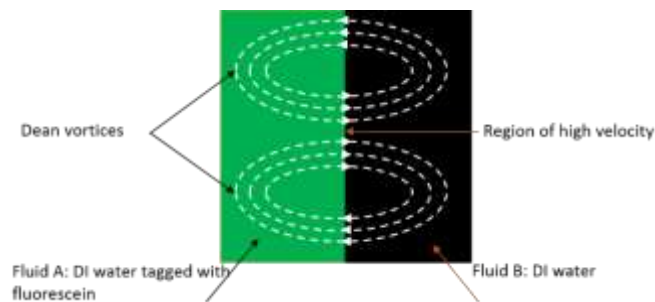
Figure 27: Illustration of flow profile and secondary flow formation
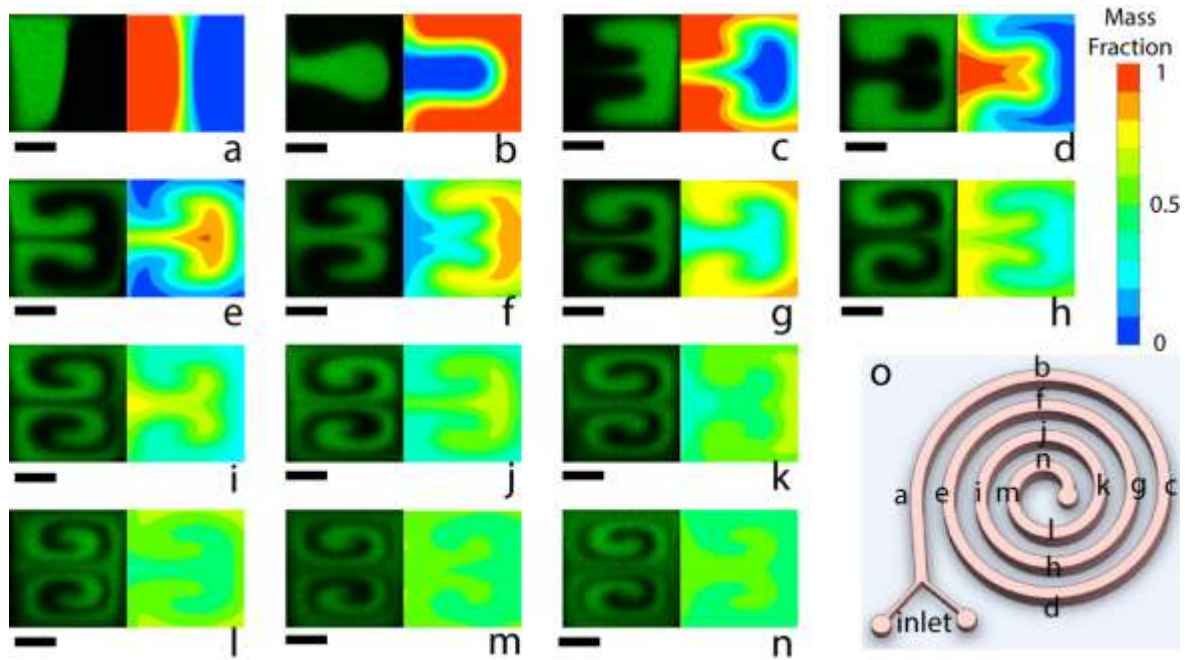
Figure 28: Illustration of the evolution of Dean vortices in the spiral microchannel from confocal microscope imaging (left) against numerically obtained results of mass fraction (right) along the length of the spiral channel, captured at every 90˚bend (a-n), as depicted in (o). For confocal microscope imaging, pure water (shown in black) and water solution with fluorescein dyes (shown in green) are introduced at the flow rate of 540 μL/min for each stream (Re=30). The dimension of the square microchannel is 600 μm x 600 μm. Scale bars for all images are 200 μm.

The formation of Dean vortices in diverse cross-sectional profiles with varying volumetric flow rates is illustrated in Figure 29, captured just prior to the outlet of the spiral microchannel (in order to avoid exit effects, position shown in Figure 28m). As observed, in a square channel (Dh = 600 μm) a low flow rate of 270 μl/min (Re = 15) is sufficient to cause initiation of Dean vortices, which then gets stronger, more prominent and stable as the volumetric flow rate is increased due to an increase in Dean number that is directly proportional to flow velocity. Time lapse images of flow at this location also indicate that these vortices are stable. At a volumetric flow rate of 270μl/min, although we see the formation of vortices these vortices do not interact with each other as in the case of Dean vortices. An increase in the spread of fluorescence concentration along the cross-section and channel length shows that the formation of Dean vortices at higher flow rates pull the two streams into each other, resulting in improved mixing performance. Although the Dean vortices start forming at a certain flow rate for all geometries, their strength and effect is more pronounced in trapezoidal and semi-circular microchannels of constant channel area, and in square

35

channels with a smaller hydraulic diameter (especially D_h = 300 µm) at a given operating flow rate. However, in the case of a 300 µm channel, the improved mixing performance can be attributed to the combined effect of diffusion and secondary vortices. These observations thereby validate that cross-sectional geometry affects the strength of the Dean vortices generated thereby enhancing mixing performance. In addition if we look at the different curvature designs as in Figure 26, we find that a spiral channel has an improved mixing in comparison to that of a serpentine or saw tooth curved channel. This can be attributed to the continuous curvature of a spiral channel with decreasing radius of curvature unlike a serpentine channel where the direction of Dean vortices are interchanged along subsequent curvatures resulting in a chaotic movement which does not aid in improving the strength of Dean vortices. Although these curvature designs have a constant hydraulic diameter, and total channel length, the radius of curvature is not the same. Plotting the variation of Dean number against Reynolds number in Figure 30, shows that the Dean number of these channels increase with an increase in the volumetric flow rate. The Dean number also increases when flow moves from the inlet to outlet. While a saw tooth and square channel have a higher radius of curvature in comparison to that of a spiral channel, these designs are not able to generate Dean vortices as observed in Figure 26 due to density of tooth in a saw tooth design while the long straight channels in a square curve are not able to sustain any vortices even if they are generated along the channel corners.

Figure 29: Cross-sectional flow profiles at the outlet (position (m) in Figure 28) of microchannels with square, tall rectangular, wide rectangular, trapezoidal and semi-circular cross-sections of constant area 0.36 mm² and square microchannels with different hydraulic diameters (300, 600, 900 µm) at different volumetric flow rates (100, 270, 540, 800 and 2000 µl/min). These images were captured using a confocal microscope at a magnification of 10x and the arrows indicate the direction of rotation as observed through time lapse imaging.
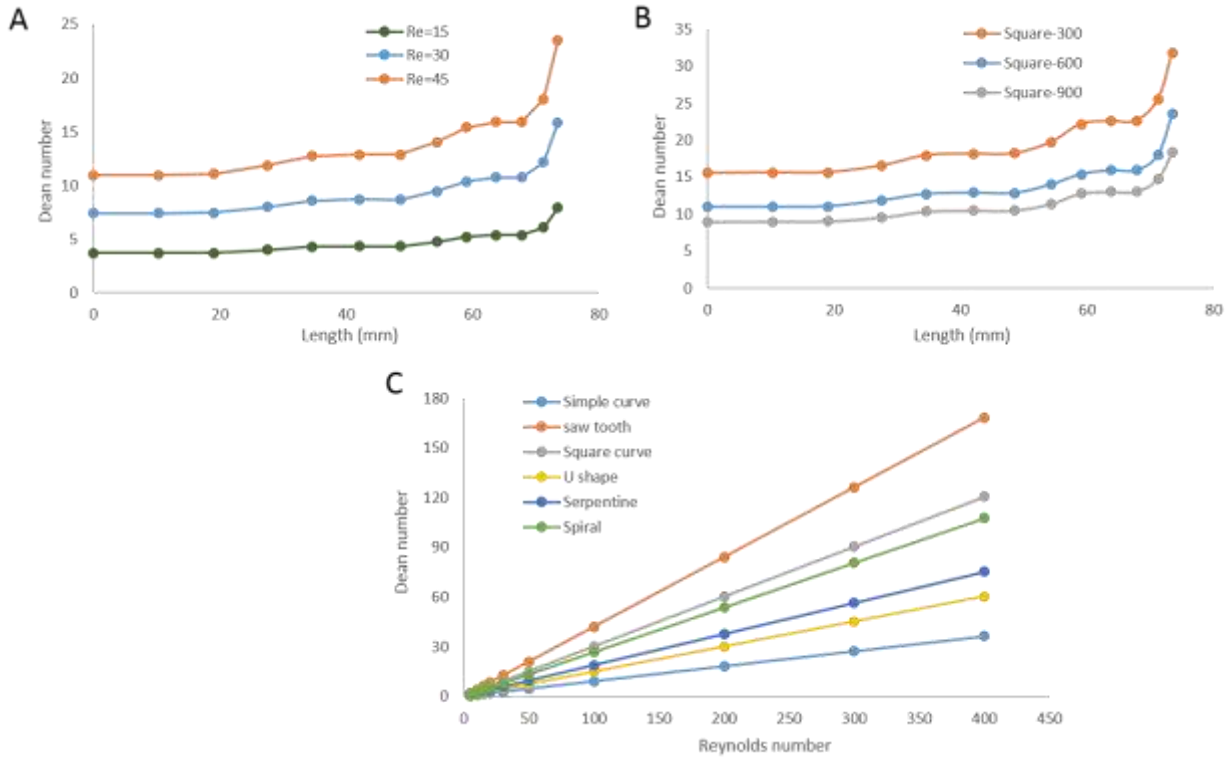
Figure 30: A) depicts the relationship between Dean number and length for a 600μm square spiral microchannel at various Reynolds numbers of 15, 30 and 45, while B) compares the variation of Dean number along the channel length for three spiral channels of varying hydraulic diameter with a square cross-section (330μm, 600μm, 900μm) at a Reynolds number of 30 and C) represents the comparison of Dean number against Reynolds for the different curvature designs in this study with the same hydraulic diameter.

3.3. Improvement in mixing performance

The visualization of the generated Dean vortices along the curved channel via confocal microscopy also allows the characterization of mixing performance along the length of the channel, as illustrated in Figure 32A. At a given flow rate, mixing in a spiral channel dramatically increases as compared with that of an equivalent straight channel (Figure 32A), due to the presence of the secondary flow along the curved channel enhancing mass transport along the transverse plane. The mixing performance at the outlet for all cross-sectional geometries obtained through confocal imaging are illustrated in Figure 32B at a flow rate of 540 µl/min (Re=30). Numerical modeling of mixing performance was also conducted and the mixing performance from these experiments correspond well with mixing performance obtained through CFD simulations run in FLUENT (Figure 31) thereby validating our numerical model. Dean flow is correlated to flow velocity and Reynolds number of the fluid (see Eqn.5), resulting in higher mixing performance at

increasing flow rate for the different cross-sectional geometry designs (Figure 32C). In Figure 32C we also observe that at a Reynolds number of 25/ Péclet (Pe) number of 10,000, the mixing performance drops and with further increase in flow velocity the mixing performance improves and reaches a stable value of above 90%. This drop in the mixing performance can be attributed to the reduced impact of convective forces in the form of Dean vortices at Re<25 where diffusion is a dominant mode of mixing, and at higher flow velocities the convective terms play a greater role resulting in higher mixing performance. The mixing performance improvement within a square microchannel of varying hydraulic diameter (300, 600 and 900 µm) at three different volumetric flow rates (270 µl/min or Re=15, 540 µl/min or Re=30 and 800 µl/min or Re=45) are depicted in Figure 32 (D-F). It is shown that a smaller hydraulic diameter generates higher mixing performance, due to higher flow velocity which results in stronger convective forces in comparison to a channel with larger hydraulic diameter. Additionally, considering a mixing performance of >90% as corresponding to a completely mixed fluid[47], total mixing can be achieved at flow rate of 540 µl/min for a 300 µm channel and at 800 µl/min for a 600 µm spiral microchannel with a square cross-section. This illustrates that mixing in spiral microchannel is effective at intermediate flow rates (Re>20) due to the formation of Dean vortices which aid the process of diffusion.
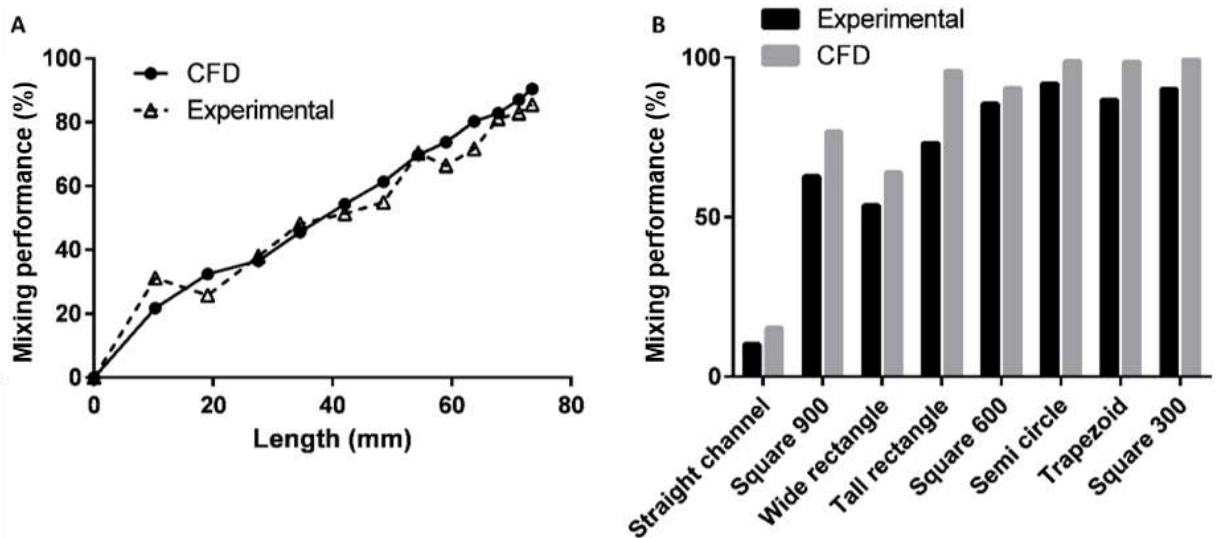
Figure 31: Comparison of experimental and numerically obtained mixing performances A) for a 600 µm x 600 µm square microchannel at 540 µl/min or Re=30 throughout the length of the channel B) at the outlet for all geometries at a flow rate of 540 µl/min or Re=30.
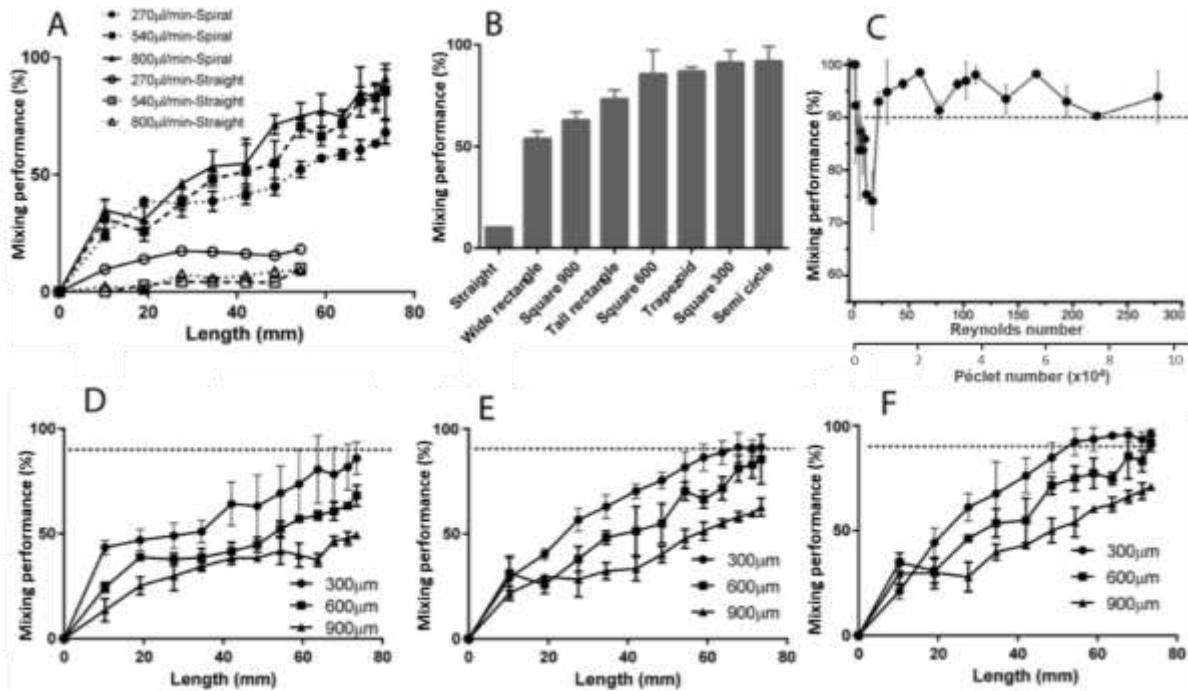
Figure 32: (A) Comparison of mixing performance in straight and spiral microchannels of square cross-sectional geometry with dimensions 600 μm x 600 μm at three different flow rates (270 μl/min or Re = 15, 540 μl/min or Re = 30 and 800 μl/min or Re = 45). (B) Mixing performance just prior to the outlet of spiral channels with different cross-sectional geometries at a flow rate of 540 μl/min (Re=30). (C) The mixing performance just prior to the outlet of 300 μm x 300 μm square microchannel over a range of Reynolds numbers and corresponding Péclet number. (D-F) Comparison of mixing performance along the length of a spiral microchannel of square cross-sectional profile with varying hydraulic diameters (300, 600 and 900 μm) at different flow rates D) 270μl/min or Re=15 E) 540μl/min or Re=30 F) 800 μl/min or Re=45. The straight horizontal dash lines indicate the mixing performance of 90%. All these results were obtained from experimental imaging studies.

Furthermore, to investigate the effect of geometry on mixing performance, the cross-sectional area of the various different geometries was fixed to obtain constant velocity, as depicted in Table 1. The mixing performances along the spiral channel for all geometries studied are shown in Figure 34. Considering the mixing performance at a point just prior to the outlet, at a given constant cross-sectional area, the trapezoidal and semi-circular shapes give higher mixing performance (5% increase) as compared to square and rectangular profiles (Figure 32B and Figure 33A-C). At a flow rate of 540 μl/min (Re=30) the mixing performance in a semi-circular channel is greater than 90%, whilst in a 600 μm square channel the same flow rate produces a mixing performance of just 85%, and in the wide rectangular channel a mixing performance of only 54%, as illustrated in Figure 32B.
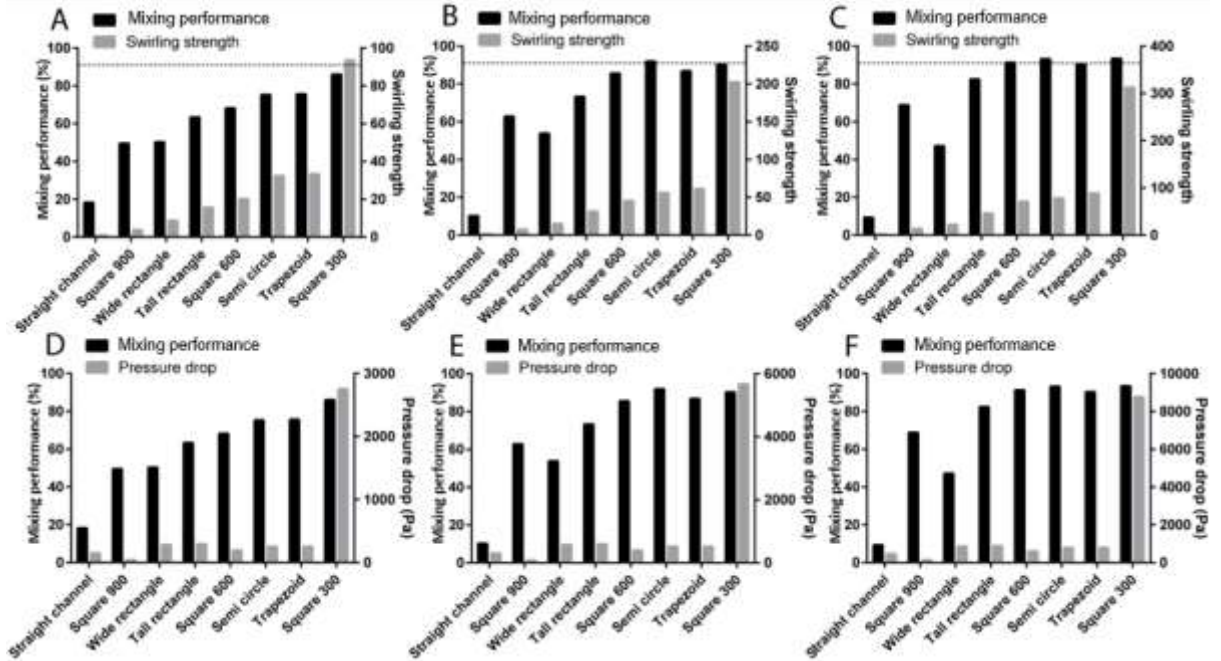
Figure 33: (A-C) Comparison of numerically obtained swirling strength and experimentally obtained mixing performance to illustrate the relationship between the two parameters at three different flow rates - A) 270 μl/min or Re = 15 B) 540 μl/min or Re = 30 C) 800μl/min or Re = 45. The dash line represents the mixing performance of 90%. (D-F) Comparison of mixing performance and pressure drop for microchannels of different cross-sectional geometries at D) 270 μl/min E) 540 μl/min F) 800 μl/min.
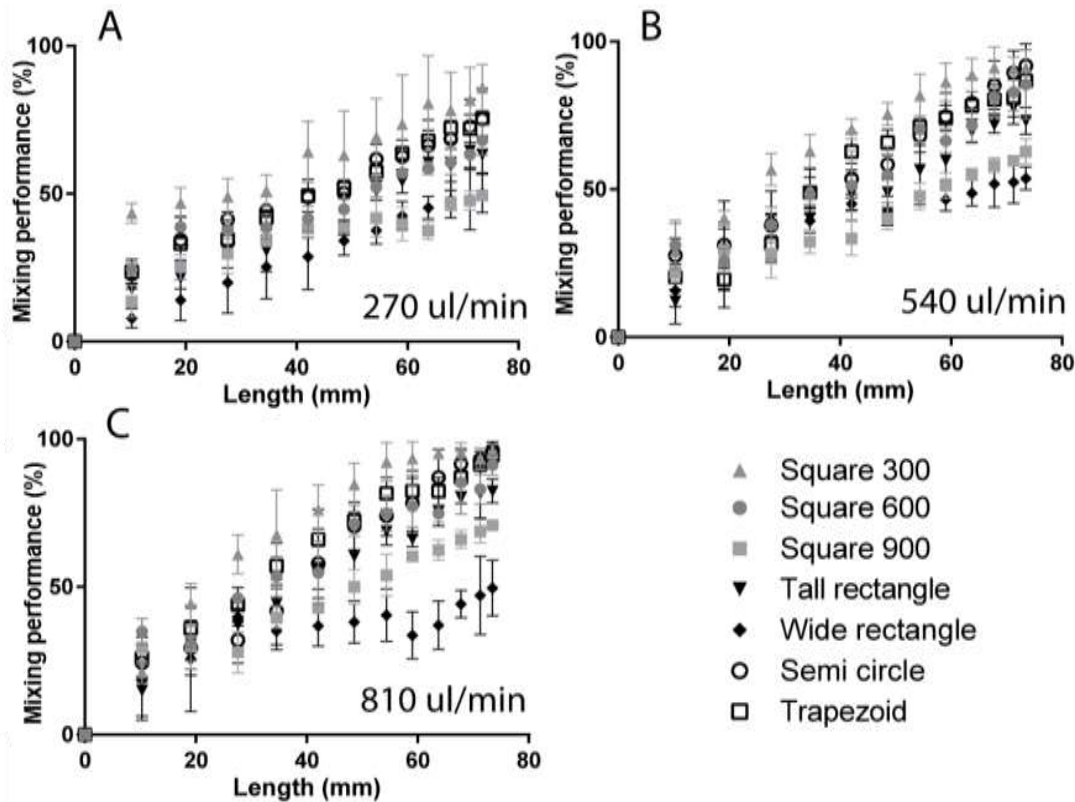
Figure 34: Mixing performance along the channel length for different geometries at three different flow rates A) 270 μl/min or Re = 15 B) 540 μl/min or Re = 30 C) 800 μl/min or Re = 45.

41
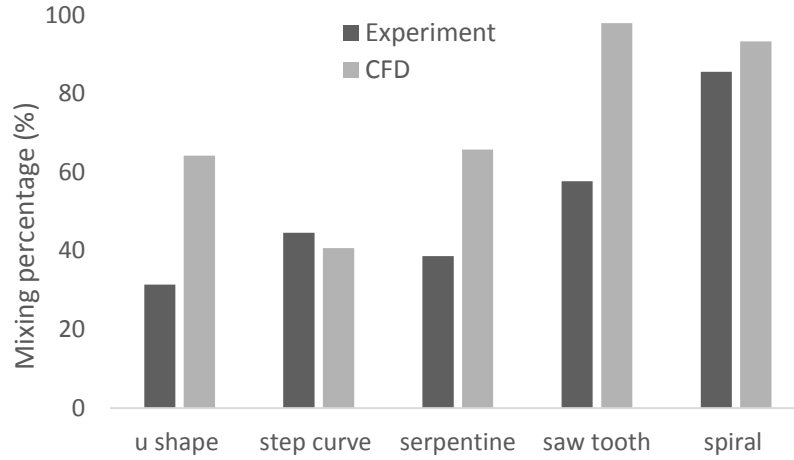
Figure 35: Comparison of mixing performance obtained numerically through CFD and experimentally obtained mixing performance for different curvature designs at a flow rate of 540µl/min (Re=30) at the outlet.

Apart from varying the cross-geometry, various variants of curvature were studied for mixing performance and we see that among all the designs the spiral channel has a superior mixing performance in comparison to a saw tooth or serpentine microchannel despite having a higher Dean number as shown in Figure 35 due to the formation of Dean vortices which enhance mixing performance in microchannels.
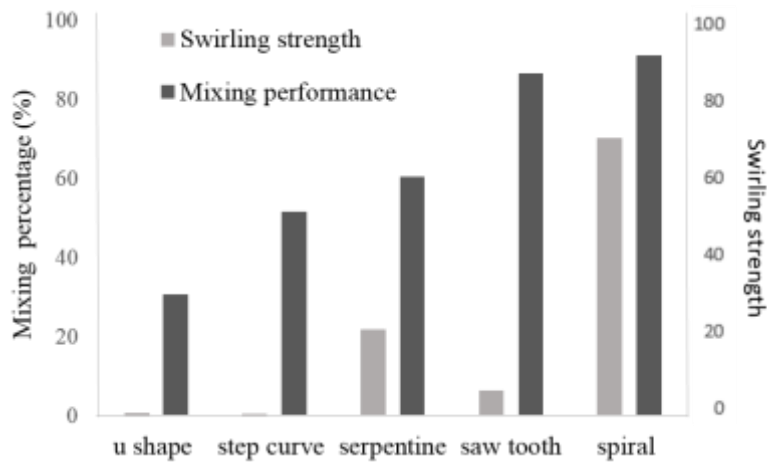
Figure 36: Experimentally obtained results of mixing performance and swirling strength for the different curvature designs at a flow rate of 800µl/min obtained at the outlet.
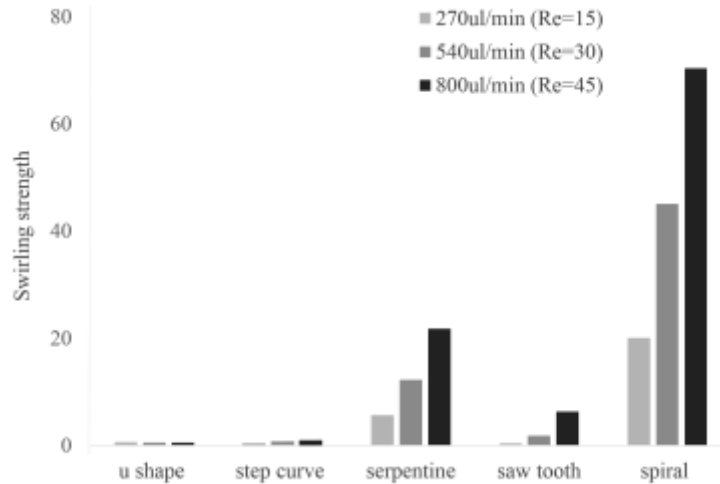
Figure 37: Comparison of swirling strength for different curvature designs at a volumetric flow rate of 270μl/min (Re=15), 540μl/min (Re=30) and 800μl/min (Re=45) obtained at the outlet.

To further understand the contributing factor towards this improved performance in semi-circular/trapezoidal geometries of a spiral channel on mixing performance, the strength of the vortices formed within a cross-section can be quantified through the swirling strength, which is a ratio of the tangential fluid velocity to the core velocity. Due to the formation of vortices within the microchannels, the velocity generated at the central core separating the two vortices is very high, resulting in higher swirling strength in all the curved channels in comparison to an equivalent straight channel as seen in Figure 33. CFD simulations can provide this information for different geometries (Figure 33 and Table 2) and different curvatures (Figure 36 and 37), showing that swirling strength is able to predict this improvement in mixing performance and Dean vortices formation obtained from our experimental studies. Additionally, the swirling strength of a straight channel is almost negligible at all flow rates (Table 2) due to the absence of Dean vortices thereby verifying the contribution of Dean vortices towards swirling strength. A comparison of the swirling strength in the different curvature designs also validate that the presence of Dean vortices contribute towards the swirling strength of flow within these channels. Comparing the swirling strength and mixing performance for the different cross-sectional geometries of a spiral channel employed at a fixed cross-sectional area, we observe a linear relationship between mixing performance and swirling strength. It is found that trapezoidal and semi-circular channels achieve the highest mixing performance due to their

increased swirling strength which can be attributed to the formation of Dean flow along the channel cross-section (Figure 33 and Table 2). These observations show that changing the cross-sectional geometry of the microchannel allows for control of the strength of Dean vortices within the fluid without impacting the pressure drop since hydraulic diameter is the key dimension that dictates the magnitude of the pressure drop, as observed in Figure 33D-F, especially for the 300 µm channel case where we see a rapid increase in pressure drop. In this way, this method can be utilized instead of the traditional approaches of varying the radius of curvature or flow rate.[17,48,49] Since swirling strength grows in magnitude when the flow velocity within the channel increases, the swirling strength in a smaller channel (300 µm) is twice as large as that of a larger channel (600 µm). This again corresponds to the results of the present experimental mixing study.

Table 4: Numerical comparison of pressure drop, swirling strength and mixing performance in microchannels of different geometries at A) 270 µl/min or Re=15 B) 540 µl/min or Re=30 C) 800 µl/min or Re=45.

Flow Rate	270 µl/min			540 µl/min			800 µl/min		
Geometry	Pressure Drop (Pa)	Swirling strength	Mixing Performance (%)	Pressure Drop (Pa)	Swirling strength	Mixing Performance (%)	Pressure Drop (Pa)	Swirling strength	Mixing Performance (%)
Straight	147	0.83	18.18	299	1.26	10.14	452	1.45	9.20
Square 900	37	3.73	49.43	74	7.41	62.76	125	13.04	68.76
Wide rectangle	279	8.60	50.17	566	14.85	53.69	851	21.75	47.10
Tall rectangle	292	15.51	63.28	588	31.19	73.19	878	45.83	82.37
Square 600	190	20.06	68.14	389	45.09	85.53	592	70.44	91.30
Semi-circle	251	32.30	75.21	513	55.92	91.89	778	77.76	93.09
Trapezoid	250	33.27	75.63	512	60.93	86.76	779	88.59	90.33
Square 300	2752	93.43	85.95	5665	202.49	90.18	8759	312.46	93.41

At various flow rates, mixing performance near the outlet of the spiral channel is correlated with Reynolds number, as illustrated in Figure 32C. As can be seen, at low Re (<1), the mixing inside the 300µm square channel is nearly complete since mixing in this flow regime is dominated by molecular diffusion, which is promoted by a long residence time and the resulting interaction of two fluids. When the flow rate increases (1<Re<20), two effects are found to occur: the higher convective flow reduces the resident time leading to decreased mixing due to diffusion, and centrifugal forces begin to generate recirculating flow in the transverse plane which can enhance mixing performance. At this relatively low Re range, the latter effect

is not significantly strong enough to perturb the axial flow, leading to a dip in the mixing performance since diffusion effects still dominate. At higher flow rates (Re>20), the centrifugal force becomes strong enough to trigger secondary flow, leading to higher mixing performance as the slower moving fluid moves from the concave (inner) to convex (outer) walls, as observed in Figure 38, where the two velocity cores are pushed towards the outer wall. In the spiral microchannels presented in this study, it can be observed that the formation of secondary flow at 20<Re<277 aids in increasing mixing performance, which is promising and appropriate for applications requiring high operating flow rates, such as industrial micro reactors and heat transfer. It is noted that in the present experiments it was not possible to operate at extremely high flow rates (Re>277) due to the limitations of the visualization instrumentation and fluidic setup. On the contrary, several microfluidic mixers reported in the literature can provide high mixing performance only at low Re (<100) 12, 15, 20 [17,47,50], limiting their usage for high-throughput systems. Moreover, most of these devices contain delicate structures, obstructions and sharp corners along the axial axis which could create an increased pressure drop and additional dead zone areas where particulate contamination and air bubbles can be trapped. The present spiral channel can instead provide homogenous fluidic flow without dead zone and fouling formation which is studied in the next section.[51]

Furthermore, from these numerical and experimental results, it can be observed that the improvement in mixing within spiral channels of varying cross sectional geometries can be explained via their relative value of swirling strength. As spiral channels produce higher values of swirling strength (and mixing performance) than the minimal swirling strength found in straight channels, it is clear that an additional component of velocity in the tangential direction generated through force imbalance is able to create forced fluidic interactions resulting in improved mixing performance. In addition, the velocity cores generated in the two halves of the channel through the formation of Dean vortices are pushed towards the outer wall, thereby driving the fluid towards the center of the channel in a recirculating fashion as validated in Figure 39. The mixing performance in a smaller channel is greater than that in a larger channel, however a 300 µm channel has a higher pressure drop (more than one order of magnitude) than that of a 600 µm channel (Table

2 and Figure 33D-F). This considerable increase in pressure drop would be a major deterrent in applications where pressure drop would be of great importance, such as an integrated lab on a chip device consisting of multifunctional units in one single device, microreactors and heat exchanger systems.
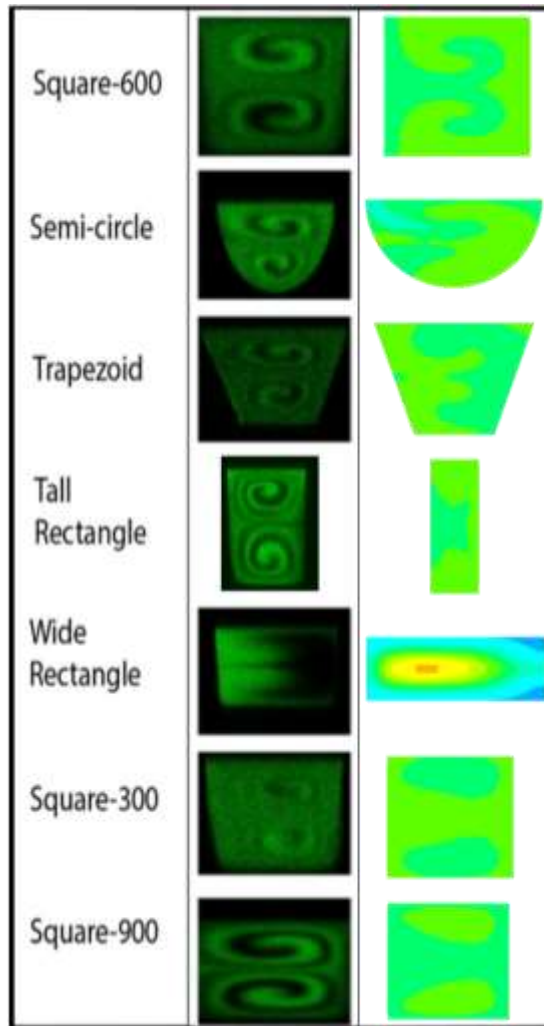
Figure 38: Cross-sectional flow profiles at the outlet (position (m) in Figure 28) of microchannels with square, tall rectangular, wide rectangular, trapezoidal and semi-circular cross-sections of constant area 0.36 mm² and with different hydraulic diameters (300, 600, 900 µm) at volumetric flow rates 800µl/min. The images on the left were captured using a confocal microscope at a magnification of 10x while those on the right depict the helicity contours obtained numerically.

In addition, the geometry of the cross-section is able to further enhance the strength of Dean vortices by providing more contact surface for rotation of Dean vortices along curvature or slopes resulting in improved mixing performance in trapezoidal and semi-circular channels. In the case of a wide channel, the vortices generated on both halves spread along the longitudinal direction causing limited interaction between the top and bottom halves of fluid flow resulting in reduced mixing performance. Similarly the non-symmetric

46

nature of irregular shapes such as trapezoid and semi-circular profiles, cause the vortices in the two halves to be non-symmetric in shape, forcing vortices in the two halves to interact with each other and match their velocities so as to maintain stability. Furthermore, the presented spiral microfluidic system is fabricated from a single layer of microfluidic chip bonded to a glass substrate, hence reducing fabrication time and potential alignment errors created in 3D structure micromixers due to the several layers and steps in the fabrication process.[33,47]

Chapter 4

Fouling in microchannels and design considerations

4.1. Experimental setup

4.1.1. Fouling experiments

Particulate fouling was studied in the different curvature design to see how Dean flow impacts fouling rate/ particle deposition during a continuous flow process. The channels were fabricated using PDMS as described above, while they were either bond to a glass surface, or PDMS sheet through plasma bonding while the channels were also bond to a sheet of metal through adhesive bonding using a silicone adhesive (Dow Corning). Flow was then introduced into the channels using a syringe pump (Syringe Pump., Inc) through Tygon tubing (1.5mm diameter) at different volumetric flow rates ranging from 0.25ml/min to 2ml/min for a duration of 90minutes. The tubing can be used at temperatures upto 185˚C while a 140ml syringe (Monoject, Kendall) was used at the extreme case of 2ml/min for a duration of 60minutes. Polystyrene particles diluted in water with small amounts of surfactant to prevent particle coagulation of diameter 0.6µm is diluted with DI water and 25µM NaCl as the working fluid to study fouling over a period of 90minutes. As the concentration of particles in the dispersion increase the rate of fouling increases due to particle-particle interaction. At this concentration the flow was introduced into the different channels while they are imaged under a fluorescence microscope (Olympus, Andor iXonEMCCD) for a duration of 90minutes for the initial set of comparison, while another set of experiments were conducted where the particles were introduced into the channels for a period of 90minutes and then imaged under this microscope upon completion of the experiments.

4.1.2. µPIV studies

In order to obtain the microchannel wall characteristics and their affinity towards particle accumulation, µPIV studies were conducted to obtain the velocity profiles in a 2D x-y direction while the Reynolds wall shear stress along the vertical direction can be obtained by changing the focal plane and imaging along this direction at different time points.
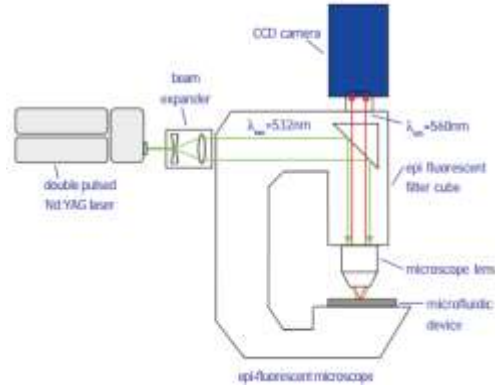
µPIV system uses a double pulsed Nd:YAG laser focused by an epifluorescent microscope onto the microfluidic device. The microfluidic system needs to be seeded with fluorescent particles with a sufficient concentration so that the flow of these particles traces the path of the fluid. A microscope lens placed below the microfluidic device collects light emitted by the particles with a wavelength larger than the illuminating light. The filter cube helps in separating the emitted light from that of the illuminating light which is thereby captured by the CCD camera. The common mode of image capturing by a µPIV system is to record two successive images separated by a time delay Δt. The image fields are separated into uniformly separated interrogation windows which are then cross correlated to determine the displacement of particles over time. In this case two size of interrogation window was chosen a 32x32 pixels slower velocities at the channel walls can be captured. The fluid velocity v, can then be determined by the relation

$$v = \frac{\Delta x}{\Delta t}$$

where Δx is the displacement of particles obtained through cross-correlation, over a given time period Δt. In this study a set of 10 images at intervals of 800ms were averaged to give the velocity profile along these microchannel designs. It is also common to use a light sheet to illuminate the particles, although this allows illumination only along the focused plane with minimal background noise. Owing to its small scales in microfluidic devices, it is hard to focus a light sheet into an area of interest, thus the light sheet illuminates the entire test section and the focus plane is obtained through the depth of field of the objective lens being used. The depth of correlation can be expressed as[52]:

49

$$z_{corelation} = 2 * \left[\left(\frac{1 - \sqrt{\varepsilon}}{\sqrt{\varepsilon}} \right) \left[\frac{d_p^2 n_1^2}{4NA^2} + \frac{5.95(M+1)^2 \lambda^2 n_1^4}{16M^2 NA^4} \right] \right]^{1/2}$$

Where ε is chosen to be 0.1 under normal circumstances. $z_{corelation}$ is highly dependent on the numerical aperture of the lens 'NA', particle size 'd_p' and the magnification of lens that is being used 'M'. Since the magnification used is 5x and particle size of 0.86µm was chosen the depth of correlation obtained is about 80µm.
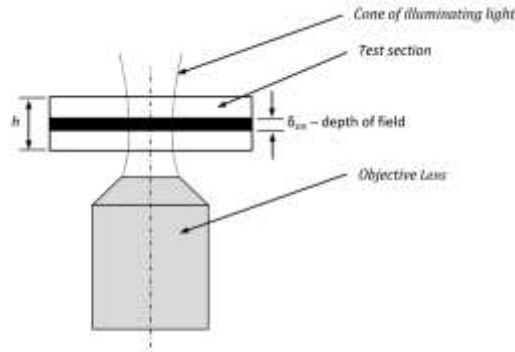
Figure 40: Illustration of the light flow path in a PIV setup

Hardware

The images are captured using a CCD camera (Dantec Hisense) with adjustable exposure time which is determined based on flow conditions and channel size of the capture area. The camera is connected to a microscope with 5x and 10x magnification, however due to the relatively small capture area under 10x magnification, the 5x magnification was used with a numerical aperture of 0.1. As the microchannel devices are made of PDMS, their transparency allows visualization from the bottom of the channel.

Post processing

While post processing, the average velocity over 10 images were obtained through an average correlation method through the in-built software so as to output the velocity vectors for the flow. Averaging over a range of images helps in improving the signal-noise ratio while minimizing the background noise. From these results the velocity plot along a given line in this plane can be obtained to validate the settings since

the flow profile should be laminar with a single parabolic curve. In addition the velocity data obtained over

the time points can be exported as a .dat, tecplot file enabling us to obtain other flow parameters such as

the Reynolds wall shear stress represented by:

$$\tau_w = \mu \frac{\partial u}{\partial x}$$

Where x is the changing in position along the measured direction while 'u' is the velocity along this line

and μ the dynamic viscosity of fluid that is being used. In this case, x is the direction tangential to the axial

flow profile.

Owing to the small scale of flow dynamics, we need to take into consideration the following parameters:

Flow/ Particle dynamics

If we assume that the particle undergoes drag based on Stokes law, the first order inertial response time of

the particle can be represented as:

$$\tau_p = \frac{\rho_p d_p^2}{18\mu}$$

If we use polystyrene particles of size 0.6µm, immersed in water the particle response would be in the order

of 10^{-8}s, which is very small in comparison to fluid flow and thus it can be ignored.

Velocity error

Since the particles are <1mm in size, we need to take into account Brownian motion of the particles under

a fluid flow which explains some of our observations. The ideal (non-Brownian) x and y displacements of

the particle in the given time frame is represented as:

$$\Delta x = u\Delta t$$

$$\Delta y = v\Delta t$$

The Brownian displacement causes the particles to deviate from its ideal streamline represented above and it is largely influenced by diffusion of particles. Due to Brownian motion the relative error of the particle velocity due to its x, y displacement is represented as the ratio of relative Brownian motion and ideal displacement given as:

$$\varepsilon_x = \frac{Browninan\ displacement\ in\ x-direction}{\Delta x} = \frac{1}{u}\sqrt{\frac{2D}{\Delta t}}$$

$$\varepsilon_y = \frac{Browninan\ displacement\ in\ y-direction}{\Delta x} = \frac{1}{v}\sqrt{\frac{2D}{\Delta t}}$$

From this equation we see that the error can be reduced by increasing the interrogation time used during imaging. The errors can also be reduced by increasing the number of particles (N) being captured in an interrogation window and averaging over these N particles since diffusive uncertainty varies as 1/N.

4.2. Fouling results along the channels

In order to succinctly differentiate the fouling resistance in these geometries, the flow rate of operation was small below 1ml/min as at higher flow rates the fouling in some of the geometries were negligible making it hard to compare them for fouling resistance induced due to geometric difference. As in the previous section where mixing performance was compared in spiral channels of different cross-sections along with various curvature designs of same hydraulic diameter as that a spiral channel, fouling resistance was also studied in these numerous designs. Since all the micro channels were fabricated from PDMS, while using the same colloidal solution of silica based microparticles, the effect of electric double layer force and colloidal effects can be ignored for the purpose of comparing different geometries for their fouling resistance. It is well understood that the shear stress of the fluid plays a major role in mitigating particle deposition due to fluidic interaction with the particles loaded in the solution. Thus the shear stress value for the different curvatures were plotted by looking at the tangential component of velocity along the channel depth to observe the effect of Dean vortices on the velocity profile. From Figure 41, it can be observed that

52

the shear stress of fluid in a saw tooth channel is the highest which should in turn result in reduced particle deposition, however in this case the spiral channel with comparable but slightly lower shear stress has a lower rate of particle deposition at this flow rate of 540µl/min. This oddity in the behavior of particle deposition could be attributed to the formation of Dean vortices in a spiral channel which help in preventing particle deposition due to its recirculating flow that has a cleaning effect when it meets the wall surface. This is also observed in the form of swirling strength observed in Figure 33 and 36, where by the presence of Dean vortices enhance swirling strength resulting in improved mixing performance and fouling resistance. While the average shear stress value just looks at the velocity gradient values, looking at the shear stress plots (velocity gradient) plot along the channel cross section can give us more insight on how the velocity profile gets altered within these channel as depicted in Figure 41.
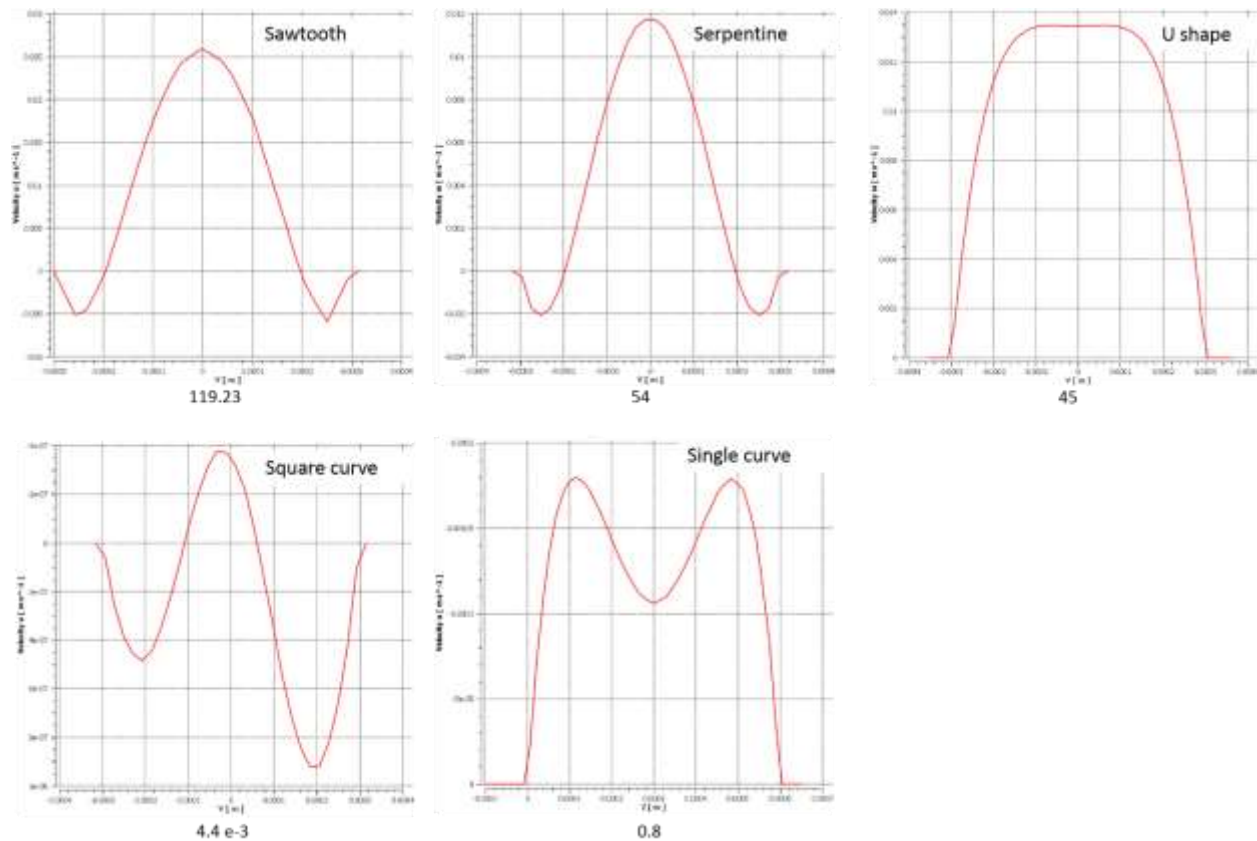

Figure 41: Tangential velocity plots for the different curvature designs plotted as a function of length obtained at a distance of 40mm from inlet. Gradient of this graph gives the shear stress experienced by flow along the channel cross section. This velocity plot is obtained along the depth of the channel through numerical studies at a flow rate of 540µl/min (Re=30)

In Figure 42, we see that among the channels with regular disturbance, spiral channel has least number of deposited particles which can be explained through the formation of Dean vortices and the varying strength of Dean vortices within the spiral channel. From Figure 43, we see that varying the concentration of NaCl changes the zeta potential of PDMS based on the relation derived by Kirby et al[53]. Thus based on equation 8 we get the electric double layer force for a PDMS surface using NaCl at a concentration of 25mM. However this value would be a constant for the different curvature designs. From Figure 44 we observe that the other curvature designs have sharp corners or a continuous change in the curvature direction which act as a trap for fluid along its flow path resulting in the formation of dead zones where fluid flow is zero. The presence of such obstructions prevent smooth flow through the channels and enhance the rate of particle deposition as observed in Figure 42. However, the behavior of the saw tooth design is an exception due its dense nature resulting in a higher shear stress of flow as it moves from one tooth to the next. This sudden change in velocity has a similar effect as that of a spiral channel.

This study of particle deposition only compares the different curvatures so as to isolate the effect of Dean vortices in providing a natural cleaning effect thereby preventing particle deposition. While comparing the variation in particle deposition among the different spiral channels with different cross-sectional geometries, the rate of particle deposition is not very high at low flow rates making it difficult to distinguish the effect of Dean strength on fouling in different cross sections.
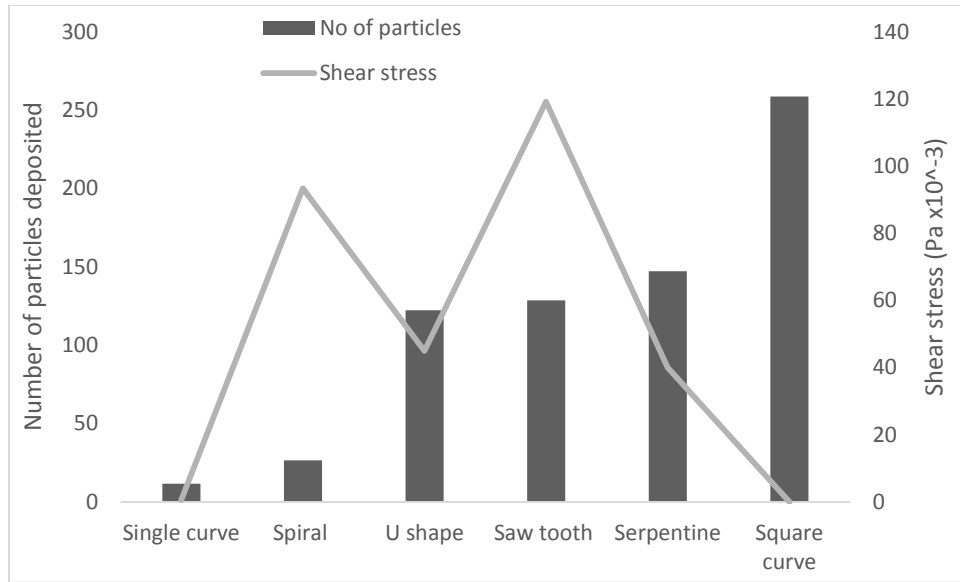
Figure 42: Relationship between shear stress introduced along the channel and the rate of fouling obtained through the number of particles deposited along the channel at a flow rate of 540µl/min (Re=30) obtained at a distance of 40mm from the inlet.
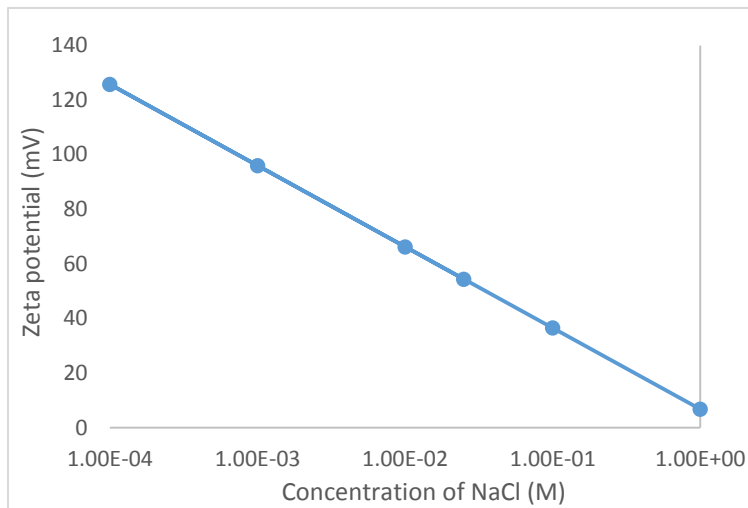
Figure 43: Variation of Zeta potential of PDMS with different concentrations of electrolyte

Table 5: Force values for the different curvature designs

	Lift force (N)	Gravity force (N)	Electric double layer force (N)
Square curve	1.45E-27	1.16E-18	-1.91E-06
Single curve	2.42E-23	1.16E-18	-1.91E-06
Serpentine	1.20E-19	1.16E-18	-1.91E-06
U shape	1.52E-19	1.16E-18	-1.91E-06
Spiral	6.55E-19	1.16E-18	-1.91E-06
Saw tooth	1.07E-18	1.16E-18	-1.91E-06
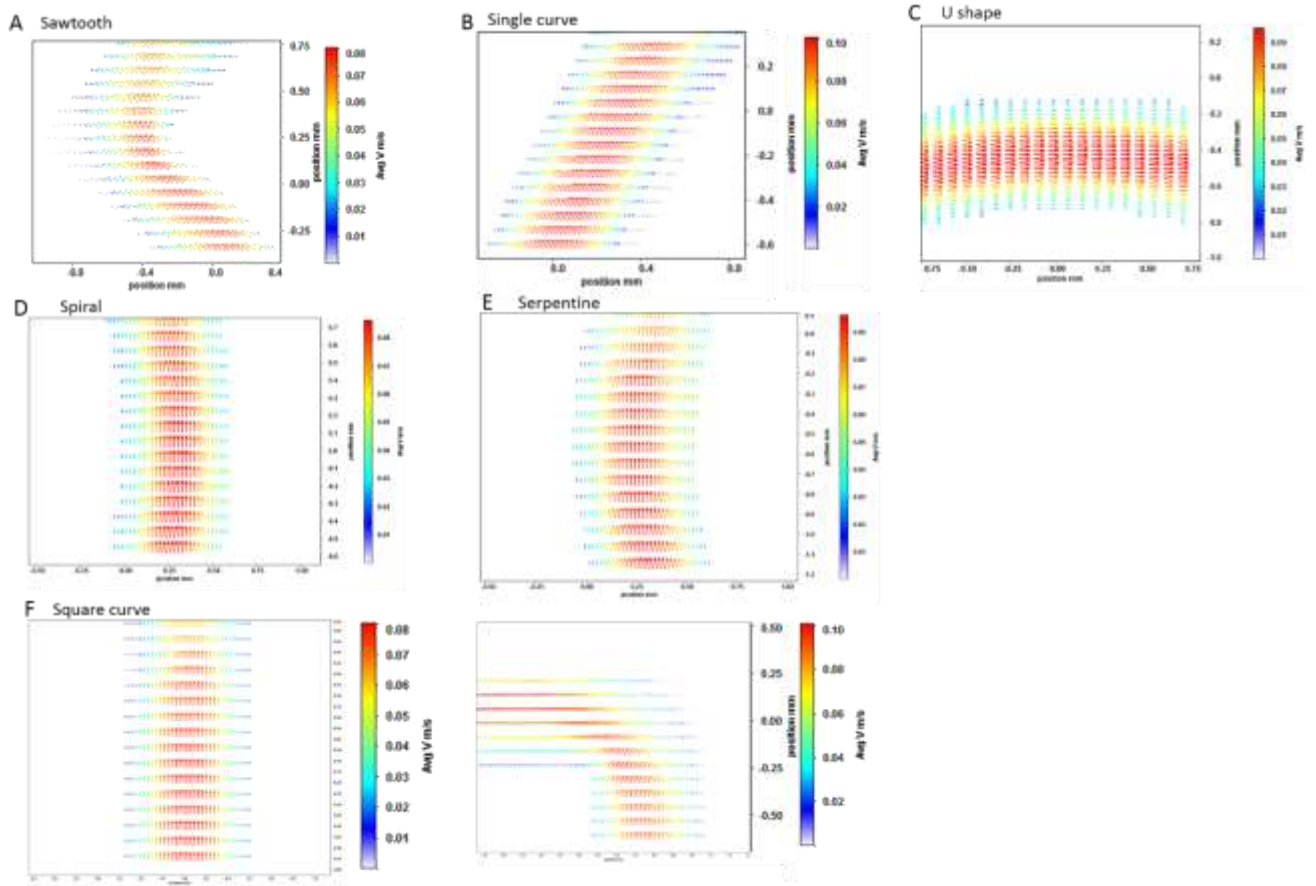
Figure 44: Velocity vector plots obtained for the different curvature designs at a flow rate of 540ul/min (Re=30) at the center most point for all designs along the center plane at a distance 40mm from the inlet for A) sawtooth curve B) single curve C) U-shape D) Spiral channel E) Serpentine F) left: Square curve along the straight section, right: along the sharp corner (90˚ bend)

Chapter 5

Conclusion and Future direction

Microchannels have gained popularity due to their high surface area per volume, thereby minimizing the amount of reagents required for a given process and making it more suitable for applications which have a limitation on the availability of sample. Through this study we have fabricated PDMS based spiral microchannels with varying cross-sectional profiles (rectangular, square, semi-circular, and trapezoidal) to study their effect on the strength of Dean vortices. It was observed that the shape of the cross section helps in dictating the strength of Dean vortices which was characterized in the form of swirling strength obtained numerically. It also shows that a trapezoidal and a semi-circular channels were able to generate stronger Dean vortices in comparison to that of a square channel of given area due to its irregularity in shape which results in mixing performance above 90% for both geometries at Re >30 at which flow velocity the effects of Dean vortices start having an effect. However, a wide rectangular channel shows the worst performance in terms of mixing performance due to its wide base and short depth thereby limiting the strength of Dean vortices. In addition for a square channel the hydraulic diameter was varied to study its impact on mixing performance. It was observed that a smaller square channel is able to generate greater mixing performance at a given volumetric flow rate due to the combined effect of diffusion and Dean vortices which get stronger at higher flow velocities. The spiral channel performance was also compared against other curvature equivalents such as the serpentine, saw tooth, square curve and U shape in terms of mixing performance, to show that the spiral channel outperforms the rest due to the formation of Dean vortices as the other channels lag behind a spiral channel in terms of swirling strength which gets stronger towards the outlet due to an increase in Dean number. The continuous turn in spiral channels aid in strengthening the Dean vortices, unlike a serpentine or saw tooth channel where the Dean vortices even if formed change their direction due to a change in curve direction.

Along with mixing performance, fouling in these channels were studied using fluorescence microscopy which shows that a spiral channel shows greater fouling resistance in comparison to the other curvature

designs. This can be attributed to the presence of Dean vortices which pulls the fluid towards the inner wall resulting in a shift of central velocity core in these microchannels. This shift in turn reduces the amount of particle deposition onto the channel walls as it carries these particles along with the flow.

The high performance and fouling-free system of the presented spiral micromixer design with an irregular cross-section of semi-circle or trapezoid are advantageous for employment in microfluidic operations (Re>20) with a requirement of low pressure drop penalties. This would be particularly useful in applications such as food, agriculture, and bio-system industries where high-throughput, high-efficiency and highly-controllable micromixers and micro reactors with cost-effective operation (low energy consumption and low maintenance frequency) [12,44,54,55] are the basis during microchannel device design.

Although this system was tested for the above mentioned applications of mixing and fouling resistance, the spiral channel performance is highly dependent on the radius of curvature employed. Thus further work needs to be conducted to establish the hydraulic diameter over radius of curvature (D_h/R) ratio for most effective improvement in mixing performance within these microchannels while limiting the rate of fouling. Another study by Sudarsan et al.[17], have shown that a spiral channel alone is not sufficient to enhance mixing performance as it increases the total channel length which in turn impacts the mixing performance, thus alternate designs of introducing expansions or bifurcations within the spiral design can be explored rather than introducing them within simple curved channels. While incorporating these designs into a spiral channel would be difficult in terms of fabrication, they can be optimized by studying the influence of curvature ratio.

BIBLIOGRAPHY

1   Weibel, D. B., Diluzio, W. R. & Whitesides, G. M. Microfabrication meets microbiology. *Nat Rev Microbiol* **5**, 209-218, doi:10.1038/nrmicro1616 (2007).

2   Lynn, N. S., Jr., Bockova, M., Adam, P. & Homola, J. Biosensor Enhancement Using Grooved Micromixers: Part II, Experimental Studies. *Analytical chemistry* **87**, 5524-5530, doi:10.1021/ac504360d (2015).

3   Chung, B. G. & Choo, J. Microfluidic gradient platforms for controlling cellular behavior. *Electrophoresis* **31**, 3014-3027, doi:10.1002/elps.201000137 (2010).

4   Lu, S. Y. *et al.* Syntheses of 11C- and 18F-labeled carboxylic esters within a hydrodynamically-driven micro-reactor. *Lab on a chip* **4**, 523-525, doi:10.1039/b407938h (2004).

5   Takeshi Iwasaki, N. K., and Jun-ichi Yoshida. Radical Polymerization Using Microflow System: Numbering-up of Microreactors and Continuous Operation. *Organic Process Research & Development* **10**, 1126-1131 (2006).

6   A.R. Oroskar, K. V. B., G. Towler. in *in: Proceedings of the VDE World Microtechnologies Congress, MICRO.tec 2000.* 385-392.

7   Veser, G. Experimental and theoretical investigation of H2 oxidation in a high temperature catalytic microreactor. *Chemical Engineering Science* **56**, 1265-1273 (2001).

8   Jeong, G. S., Chung, S., Kim, C.-B. & Lee, S.-H. Applications of micromixing technology. *Analyst* **135**, 460-473, doi:10.1039/B921430E (2010).

9   Pease, D. B. T. a. R. F. W. High performance heat sinking for VLSI. *IEEE Electron Device Letters* **2**.

10   Bashir, M., Chunangad, K. S. & Venkateswaran, P. in *Heat Exchanger Fouling and Cleaning: Fundamentals and Applications*   (2003).

11   STEINHAGEN, R., MÜLLER-STEINHAGEN, H. & MAANI, K. Problems arid Costs due to Heat Exchanger Fouling in New Zealand Industries. *Heat Transfer Engineering* **14**, 19-30 (1993).

12   Hartman, R. L. Managing Solids in Microreactors for the Upstream Continuous Processing of Fine Chemicals. *Organic Process Research & Development* **16**, 870-887, doi:10.1021/op200348t (2012).

13   Jang, L.-S., Chao, S.-H., Holl, M. R. & Meldrum, D. R. Resonant mode-hopping micromixing. *Sensors and Actuators A: Physical* **138**, 179-186, doi:10.1016/j.sna.2007.04.052 (2007).

14   Zahn, J. D. & Reddy, V. Two phase micromixing and analysis using electrohydrodynamic instabilities. *Microfluidics and nanofluidics* **2**, 399-415, doi:10.1007/s10404-006-0082-y (2006).

15   Baratunde A. Cola, D. K. S., Timothy S. Fisher, and Mark A. Stremler. A Pulsed Source-Sink Fluid Mixing Device. *JOURNAL OF MICROELECTROMECHANICAL SYSTEMS,* **15**, 259-266 (2006).

16   Qian, S. & Bau, H. Magneto-hydrodynamic stirrer for stationary and moving fluids. *Sensors and Actuators B: Chemical* **106**, 859-870, doi:10.1016/j.snb.2004.07.011 (2005).

17   Sudarsan, A. P. & Ugaz, V. M. Multivortex micromixing. *Proceedings of the National Academy of Sciences of the United States of America* **103**, 7228-7233, doi:10.1073/pnas.0507976103 (2006).

18   G. Bessoth, F., J. deMello, A. & Manz, A. Microstructure for efficient continuous flow mixing. *Analytical Communications* **36**, 213-215, doi:10.1039/A902237F (1999).

19   Schonfeld, F., Hessel, V. & Hofmann, C. An optimised split-and-recombine micro-mixer with uniform chaotic mixing. *Lab on a chip* **4**, 65-69, doi:10.1039/b310802c (2004).

20   Chen, H. & Meiners, J.-C. Topologic mixing on a microfluidic chip. *Applied Physics Letters* **84**, 2193, doi:10.1063/1.1686895 (2004).

21   Lee, S. W., Kim, D. S., Lee, S. S. & Kwon, T. H. A split and recombination micromixer fabricated in a PDMS three-dimensional structure. *Journal of Micromechanics and Microengineering* **16**, 1067-1072, doi:10.1088/0960-1317/16/5/027 (2006).

22   Song, H., Tice, J. D. & Ismagilov, R. F. A Microfluidic System for Controlling Reaction Networks in Time. *Angewandte Chemie International Edition* **42**, 768-772, doi:10.1002/anie.200390203 (2003).

23   Günther, A., Jhunjhunwala, M., Thalmann, M., Schmidt, M. A. & Jensen, K. F. Micromixing of Miscible Liquids in Segmented Gas−Liquid Flow. *Langmuir* **21**, 1547-1555, doi:10.1021/la0482406 (2005).

24   Stroock, A. D. *et al.* Chaotic mixer for microchannels. *Science* **295**, 647-651, doi:DOI 10.1126/science.1066238 (2002).

25   Liu, Y. Z., Kim, B. J. & Sung, H. J. Two-fluid mixing in a microchannel. *International Journal of Heat and Fluid Flow* **25**, 986-995, doi:10.1016/j.ijheatfluidflow.2004.03.006 (2004).

26   Howell, P. B., Jr. *et al.* A microfluidic mixer with grooves placed on the top and bottom of the channel. *Lab on a chip* **5**, 524-530, doi:10.1039/b418243j (2005).

27   Rudyak, V. & Minakov, A. Modeling and Optimization of Y-Type Micromixers. *Micromachines* **5**, 886-912, doi:10.3390/mi5040886 (2014).

28   Kim, D. S., Lee, I. H., Kwon, T. H. & Cho, D.-W. A barrier embedded Kenics micromixer. *Journal of Micromechanics and Microengineering* **14**, 1294-1301, doi:10.1088/0960-1317/14/10/002 (2004).

29   Liu, R. H. *et al.* Passive mixing in a three-dimensional serpentine microchannel. *J Microelectromech S* **9**, 190-197, doi:10.1109/84.846699 (2000).

30   Guan, G. *et al.* Spiral microchannel with rectangular and trapezoidal cross-sections for size based particle separation. *Scientific reports* **3**, 1475, doi:10.1038/srep01475 (2013).

31   Nguyen, J. Z. W. L. M. L. G. A. N.-T. Particle inertial focusing and its mechanism in a serpentine microchannel. *Microfluidics and nanofluidics* **17**, 305-316 (2014).

32   Scherr, T. *et al.* A Planar Microfluidic Mixer Based on Logarithmic Spirals. *Journal of micromechanics and microengineering : structures, devices, and systems* **22**, 55019, doi:10.1088/0960-1317/22/5/055019 (2012).

33   Yang, J., Qi, L., Chen, Y. & Ma, H. M. Design and Fabrication of a Three Dimensional Spiral Micromixer. *Chinese J Chem* **31**, 209-214, doi:10.1002/cjoc.201200922 (2013).

34   Bertsch, A., Heimgartner, S., Cousseau, P. & Renaud, P. Static micromixers based on large-scale industrial mixer geometry. *Lab on a chip* **1**, 56-60, doi:10.1039/B103848F (2001).

35   Epstein, N. Thinking about Heat Transfer Fouling: A 5×5 Matrix. *Heat Transfer Engineering* **4**, 43-56, doi:10.1080/01457638108939594 (1983).

36   Baier, R. E. in *Fouling of Heat Transfer Equipment*   (eds E.F.C. Somerscales & J.G. Knudsen, Eds) 293-304 (Hemisphere Publishing Corp, 1981).

37   Papavergos, P. G. & Hedley, A. B. Particle Deposition Behavior from Turbulent Flows. *Chemical Engineering Research and Design* **62**, 275-295 (1984).

38   Yan, Z., Huang, X. & Yang, C. Deposition of colloidal particles in a microchannel at elevated temperatures. *Microfluidics and nanofluidics* **18**, 403-414, doi:10.1007/s10404-014-1448-1 (2014).

39   Gregory, J. Approximate Expressions for Retarded van der Waals Interaction. *Journal of Colloid and Interface Science* **83**, 138-145 (1981).

40   Suzuki, A., Ho, N. F. H. & Higuchi, W. I. Predictions of the Particle Size Distribution Changes in Emulsions and Suspensions by Digital Computation. *Journal of Colloid and Interface Science* **29**, 552-564 (1969).

41   Perry, J. L. *Fouling in silicon microchannel designs used for IC chip cooling and its mitigation* Doctor of Philosophy thesis, Rochester Institute of Technology, (2007).

42   Leighton;, D. & Acrivos, A. The lift on a small sphere touching a plane in the presence of a simple shear flow *Journal of Applied Mathematics and Physics* **36** (1985).

43   Loo, C. E. & Bridgwater, J. Theory of thermal stresses and deposit removal. *Powder Technology* **42**, 55-65 (1985).

44   Schoenitz, M., Grundemann, L., Augustin, W. & Scholl, S. Fouling in microstructured devices: a review. *Chemical Communications* **51**, 8213-8228, doi:10.1039/c4cc07849g (2015).

45   Mwaba, M. G., Rindt, C. C. M., Van Steenhoven, A. A. & Vorstman, M. A. G. Experimental Investigation of CaSO4Crystallization on a Flat Plate. *Heat Transfer Engineering* **27**, 42-54, doi:10.1080/01457630500458187 (2006).

46   Kern, D. & Seaton, R. A theoretical analysis of thermal surface fouling. *British Chemical Engineering* **4**, 258--262 (1959).

47   Yasui, T. *et al.* Microfluidic baker's transformation device for three-dimensional rapid mixing. *Lab on a chip* **11**, 3356-3360, doi:10.1039/C1LC20342H (2011).

48   Sudarsan, A. P. & Ugaz, V. M. Fluid mixing in planar spiral microchannels. *Lab on a chip* **6**, 74-82, doi:10.1039/b511524h (2006).

49   Verma, M. K. S., Ganneboyina, S. R., Vinayak, R. R. & Ghatak, A. Three-dimensional multihelical microfluidic mixers for rapid mixing of liquids. *Langmuir* **24**, 2248-2251, doi:10.1021/la702895w (2008).

50   Johnson, T. J., Ross, D. & Locascio, L. E. Rapid microfluidic mixing. *Analytical chemistry* **74**, 45-51, doi:10.1021/ac010895d (2002).

51   Genic, S. B., Jacimovic, B. M., Jaric, M. S. & Budimir, N. J. Analysis of fouling factor in district heating heat exchangers with parallel helical tube coils. *International Journal of Heat and Mass Transfer* **57**, 9-15, doi:10.1016/j.ijheatmasstransfer.2012.09.060 (2013).

52   Christopher, J. B., Michael, G. O. & Gorby, A. D. Validation of an analytical solution for depth of correlation in microscopic particle image velocimetry. *Measurement Science and Technology* **15**, 318 (2004).

53   Kirby, B. J. & Jr., E. F. H. Zeta potential of microfluidic substrates: 1. Theory, experimental techniques, and effects on separations. *Electrophoresis* **25**, 187-202 (2004).

54   Neethirajan, S. *et al.* Microfluidics for food, agriculture and biosystems industries. *Lab on a chip* **11**, 1574-1586, doi:10.1039/c0lc00230e (2011).

55   Kockmann, N., Engler, M. & Woias, P. Particulate fouling in Micro-structured devices. *Proceedings of 6th International Conference on Heat Exchanger Fouling and Cleaning - Challenges and Opportunities, Editors Hans Müller-Steinhagen, M. Reza Malayeri, and A. Paul Watkinson, Engineering Conferences International, Kloster Irsee, Germany, June 5 - 10, 2005* (2005).

56.   Retrieved from https://www.softmatter.ph.tum.de/fileadmin/w00bdg/www/pdf/Vorl2_150414.pdf

57.   Retrieved from http://www.substech.com/dokuwiki/doku.php?id=stabilization_of_colloids

APPENDIX
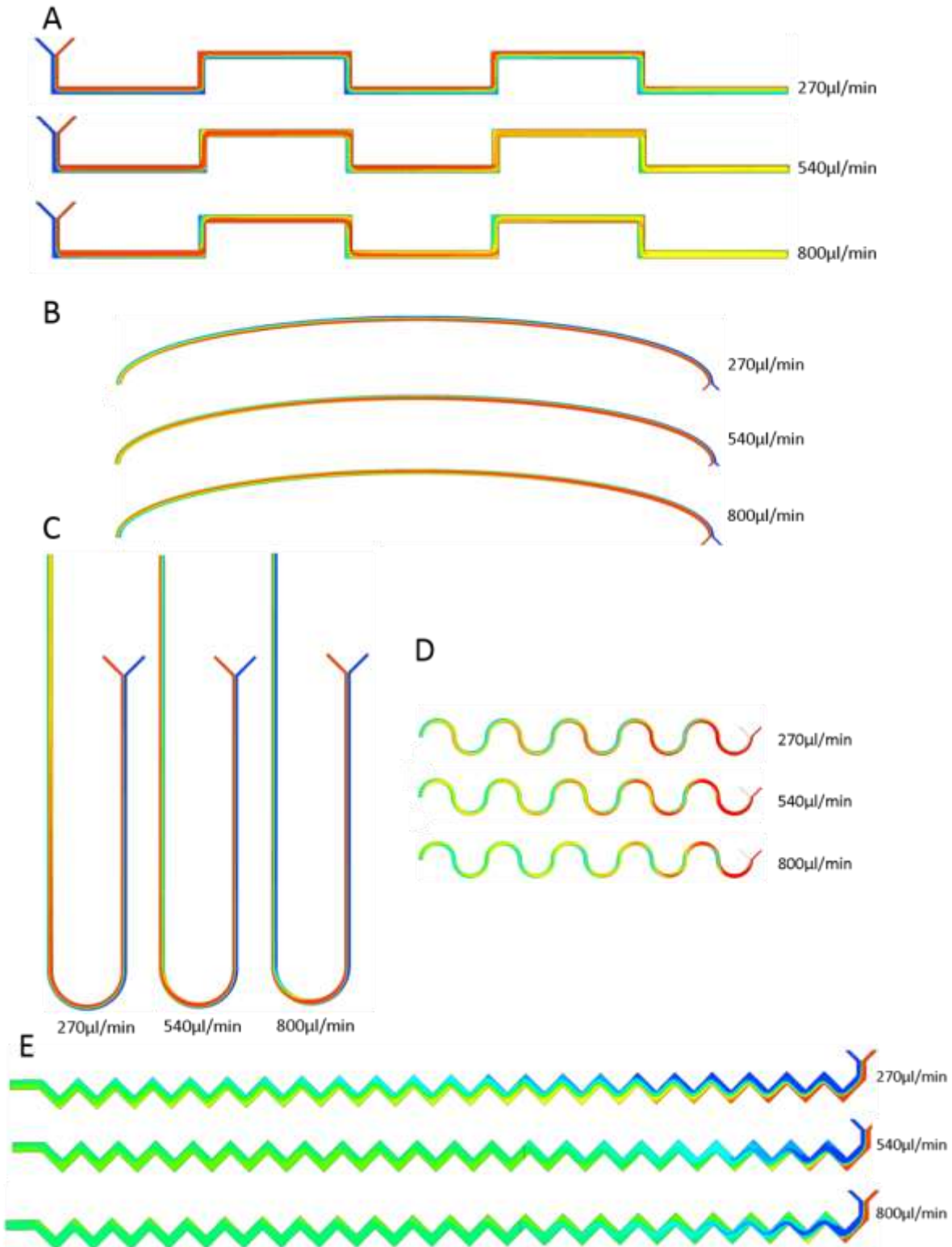
Figure 45: Mass fraction along the channel length at different flow rates of 270ul/min (Re=15), 540ul/min (Re=30) and 800ul/min (Re=45) for A)square curve microchannel B)a simple curve C) U-shape D) serpentine E) sawtooth channels
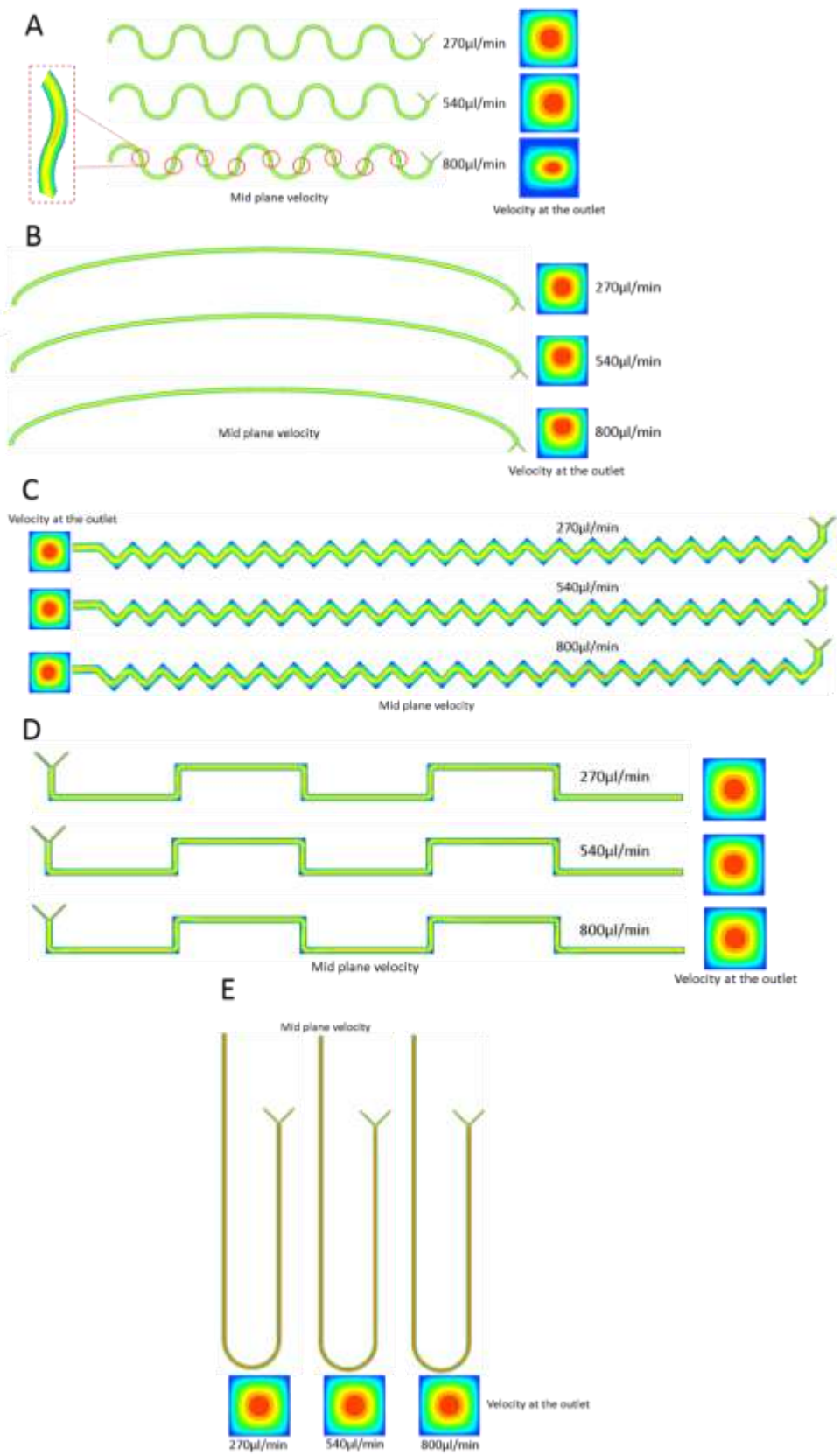
Figure 46: Velocity profiles along the mid plane of the channels A) serpentine B) single curve C) sawtooth D) square curve and E) U-shape channel
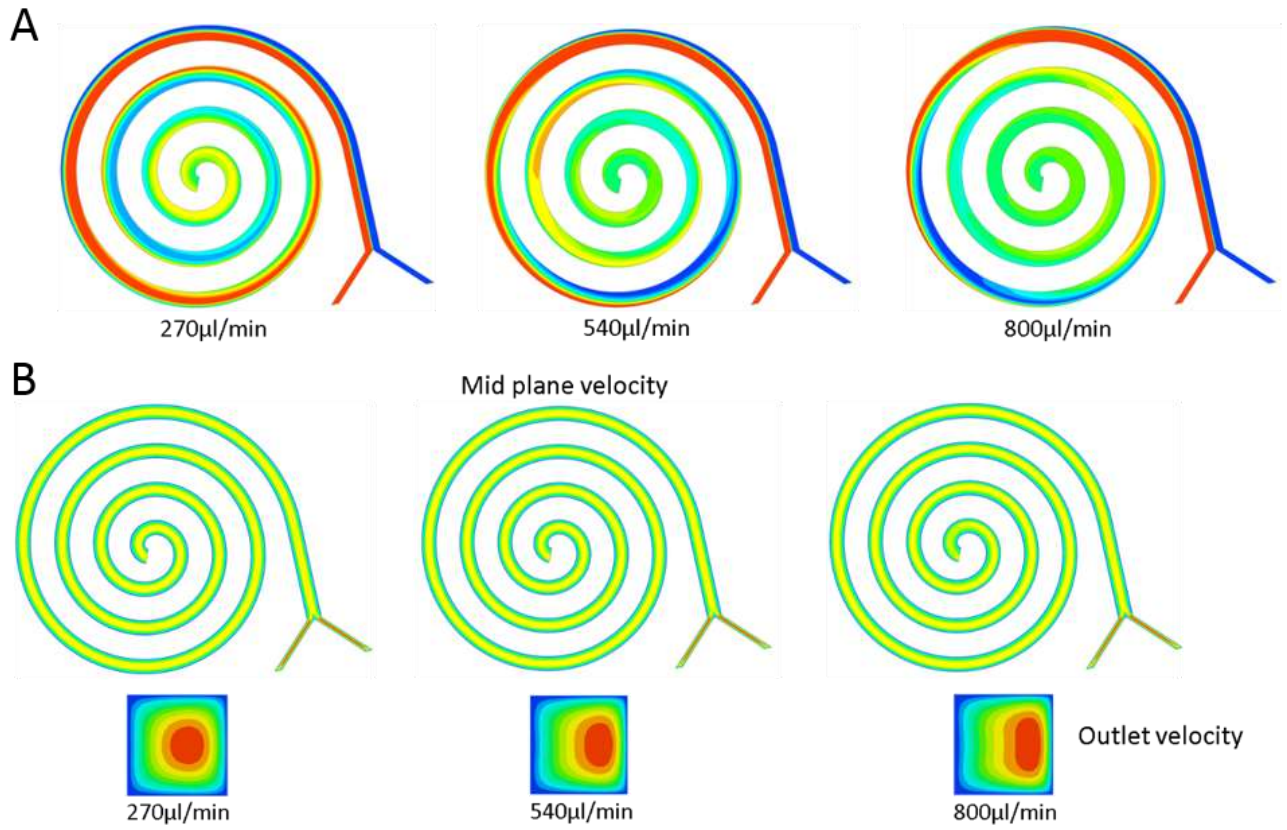
Figure 47: A) Mass fraction profile along the length of a spiral channel B) Mid plane velocity along the channel length at different flow rates
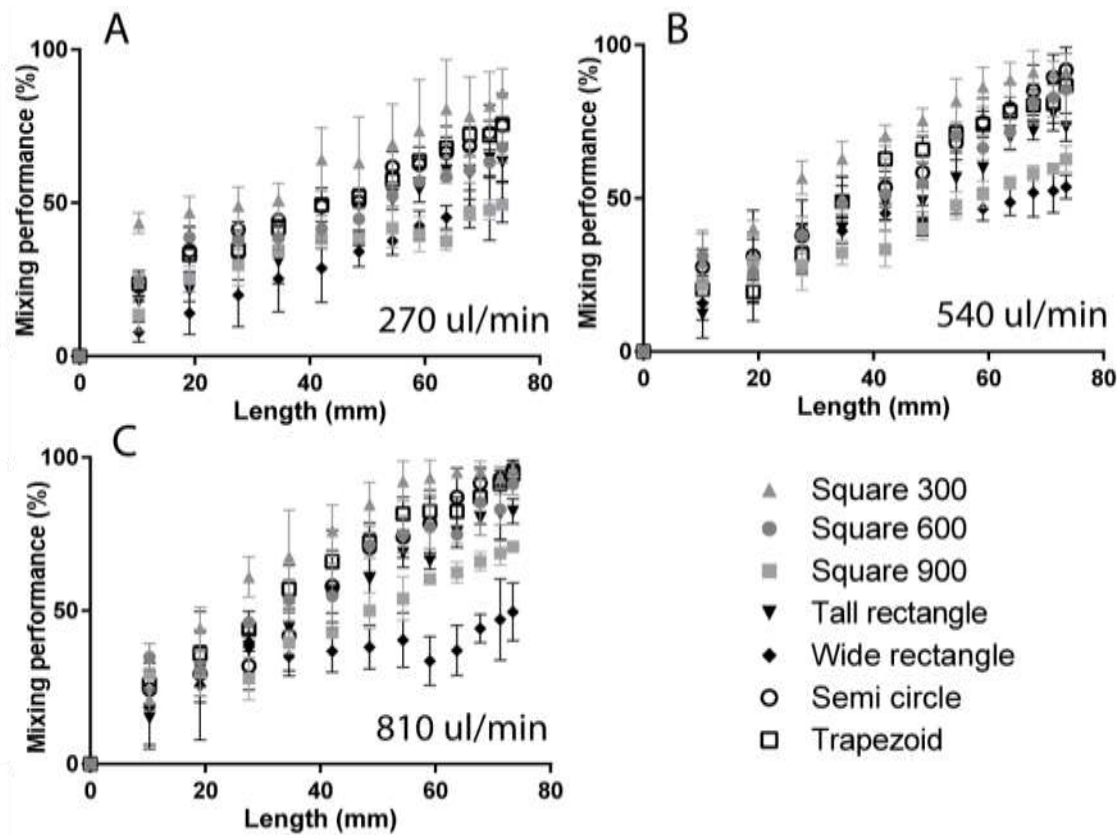
Figure 48: Mixing performance along the channel length for different geometries at three different flow rates A) 270 µl/min or Re = 15 B) 540 µl/min or Re = 30 C) 800 µl/min or Re = 45.
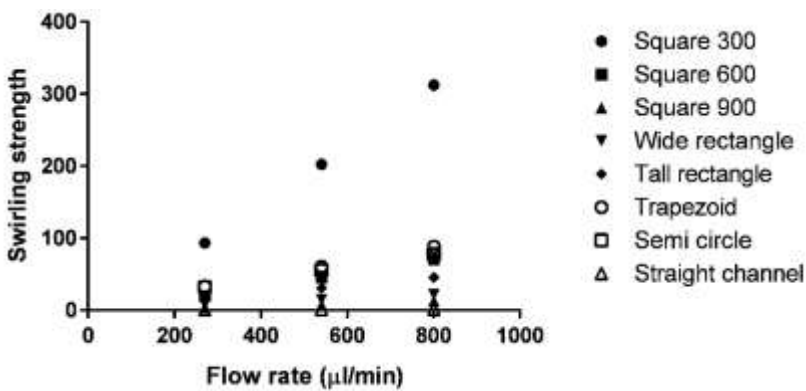
Figure 49: Swirling strength for different geometries at different flow rates obtained at location (m) in Figure 28.
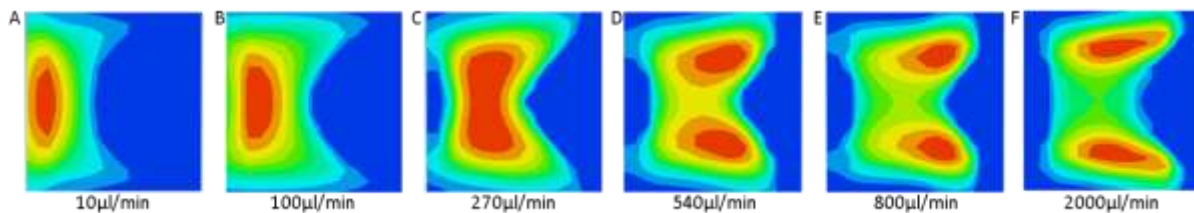
Figure 50: Swirling strength contours for a 600 µm x 600 µm square microchannel at A) 10 µl/min B) 100 µl/min C) 270 µl/min D) 540 µl/min E) 800 µl/min F) 2000 µl/min at a plane along the depth at position (m) in Figure 28.

43.75   95.83   106.25   119.23

120.83   95.83   110.41   208.33

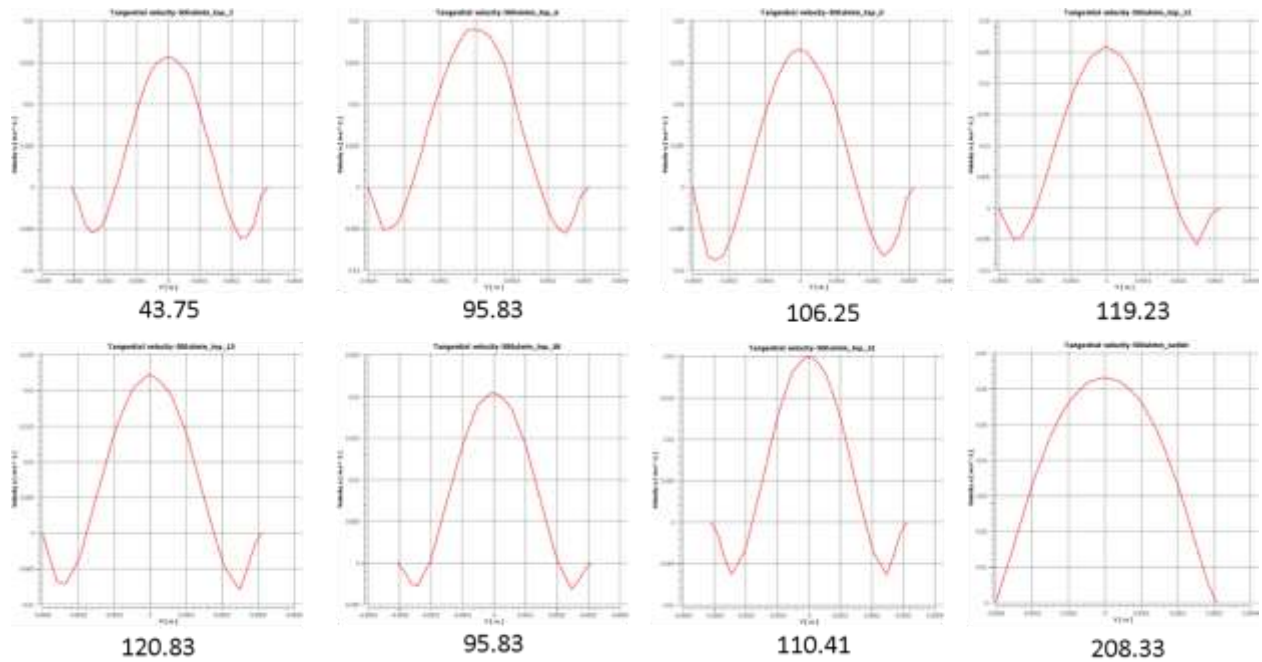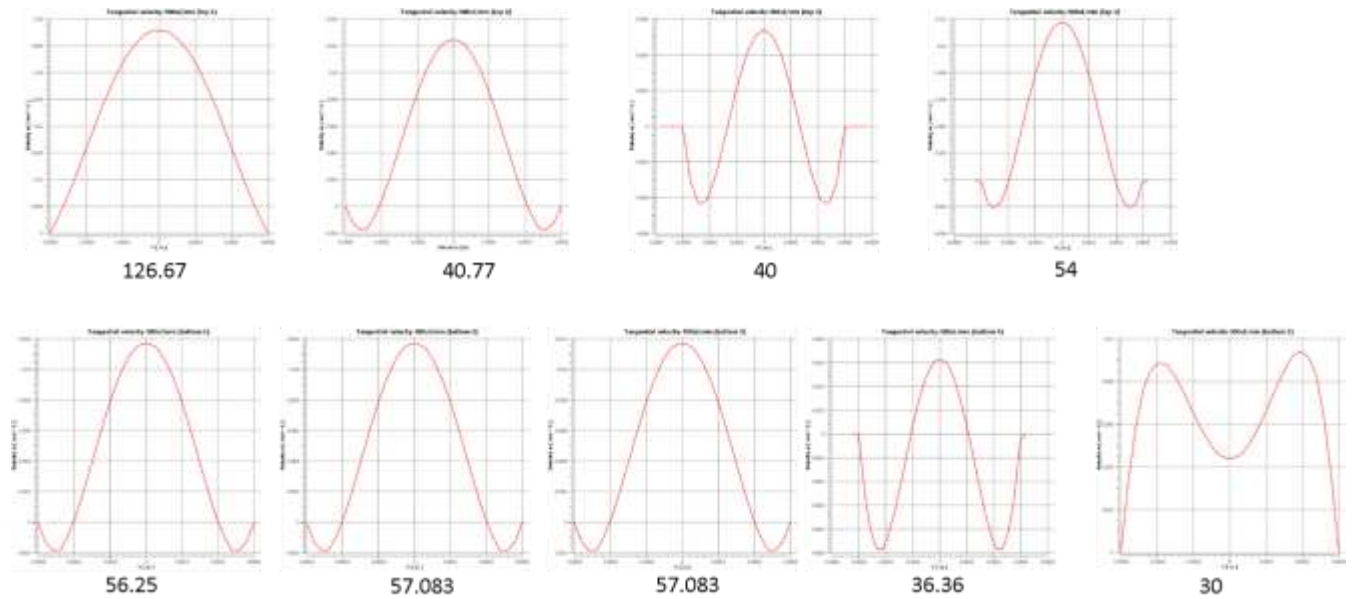*Figure 51: Shear stress profiles obtained through numerically studies along the channel depth for a saw tooth channel at a volumetric flow rate of 540µl/min (Re=30)*

126.67   40.77   40   54

56.25   57.083   57.083   36.36   30

Figure 52: Shear stress profiles obtained through numerically studies along the channel depth for a serpentine channel at a volumetric flow rate of 540µl/min (Re=30)

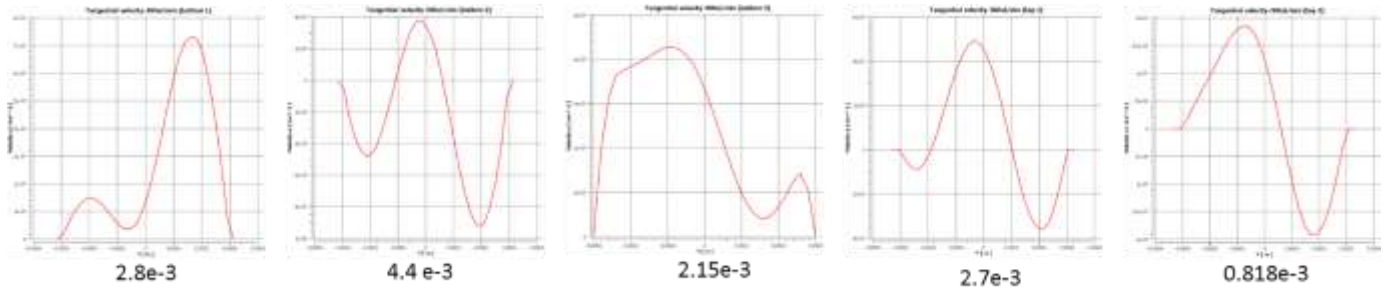2.8e-3   4.4 e-3   2.15e-3   2.7e-3   0.818e-3

Figure 53: Shear stress profiles obtained through numerically studies along the channel depth for a square curve at a volumetric flow rate of 540μl/min (Re=30)
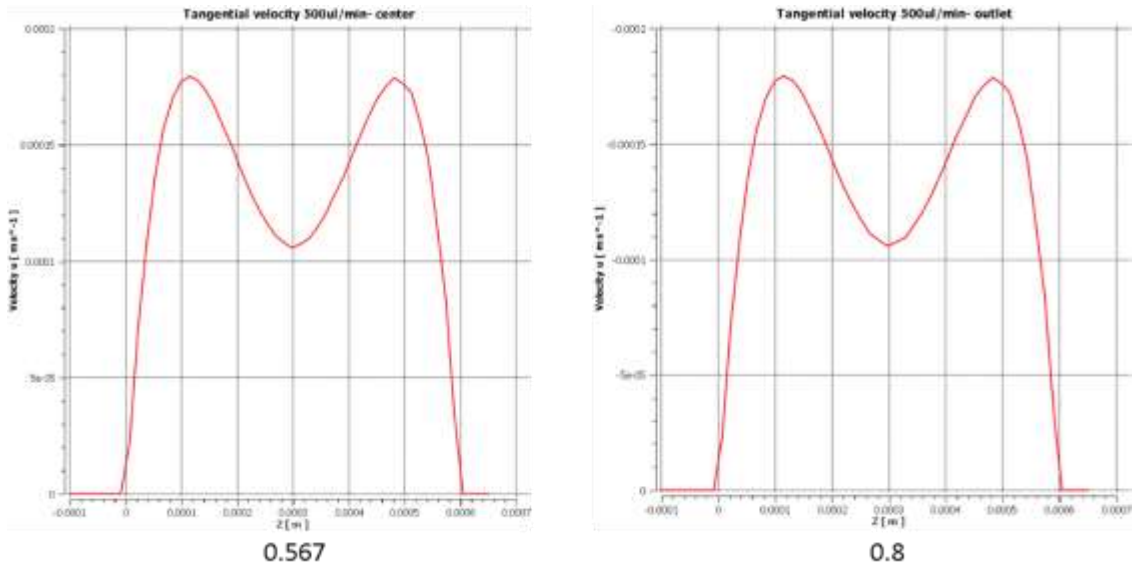

0.567   0.8

Figure 54: Shear stress profiles obtained through numerically studies along the channel depth for a single curved channel at a volumetric flow rate of 540μl/min (Re=30)
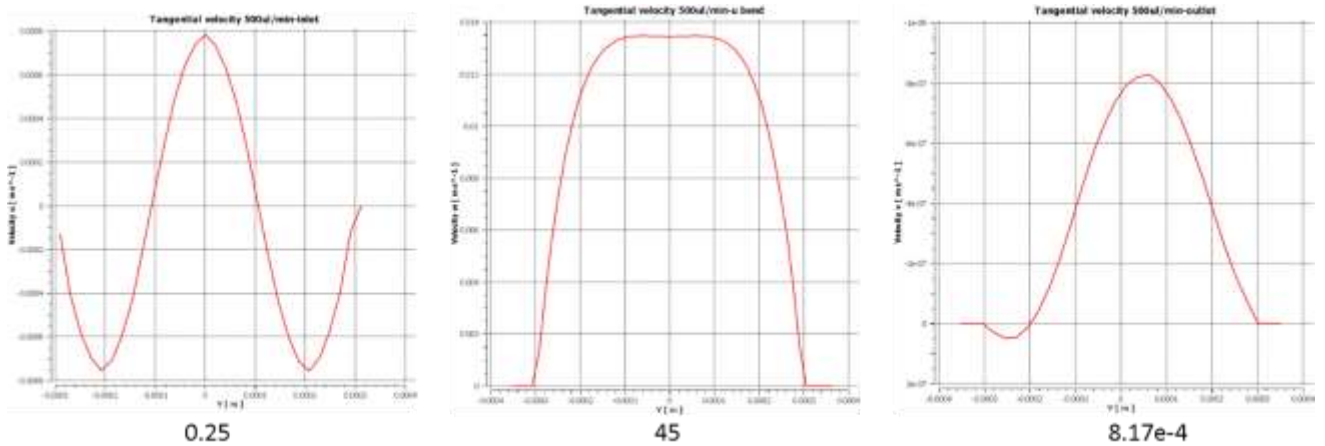

0.25   45   8.17e-4

Figure 55: Shear stress profiles obtained through numerically studies along the channel depth for a U-shaped channel at a volumetric flow rate of 540μl/min (Re=30)
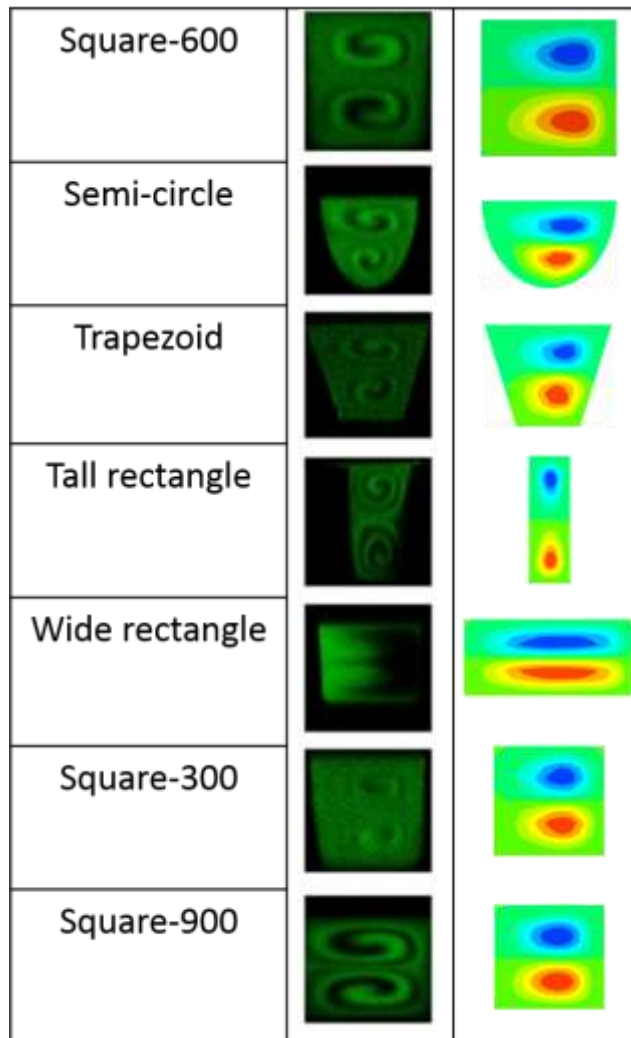
Figure 56: Cross-sectional flow profiles at the outlet (position (m) in Figure 28) of microchannels with square, tall rectangular, wide rectangular, trapezoidal and semi-circular cross-sections of constant area 0.36 mm² and with different hydraulic diameters (300, 600, 900 μm) at different volumetric flow rates (100, 270, 540, 800 and 2000 μl/min). The images on the left were captured using a confocal microscope at a magnification of 10x while those on the right depict the helicity contours obtained numerically.